Mechanical properties of bi- and poly-crystalline ice

Cao, Pinqiang; Wu, Jianyang; Zhang, Zhisen; Fang, Bin; Peng, Li; Li, Tianshu; Vlugt, Thijs J.H.; Ning, Fulong

Important note
To cite this publication, please use the final published version (if applicable).
Please check the document version above.

Mechanical properties of bi- and poly-crystalline ice

Pinqiang Cao, Jianyang Wu, Zhisen Zhang, Bin Fang, Li Peng, Tianshu Li, Thijs J. H. Vlugt, and Fulong Ning

---

Articles you may be interested in

Influence of trace water on decomposition mechanism of c-C_4F_8 as environmental friendly insulating gas at high temperature
AIP Advances **8**, 125202 (2018); 10.1063/1.5044751

Effective degradation of oil pollutants in water by hydrodynamic cavitation combined with electrocatalytic membrane
AIP Advances **8**, 125308 (2018); 10.1063/1.5028152

Live cells assessment of opto-poration by a single femtosecond temporal airy laser pulse
AIP Advances **8**, 125105 (2018); 10.1063/1.5049678

First-principles study of structural phase transformation and dynamical stability of cubic AlN semiconductors
AIP Advances **8**, 125006 (2018); 10.1063/1.5054697

Thermoelectric properties of $Ni_{0.05}Mo_3Sb_{5.4}Te_{1.6}$ composites with NiSb nanocoating
AIP Advances **8**, 125304 (2018); 10.1063/1.5038675

Synergistic treatment of SF_6 by dielectric barrier discharge/γ-Al_2O_3 catalysis
AIP Advances **8**, 125109 (2018); 10.1063/1.5054729

Mechanical properties of bi- and poly-crystalline ice

Pinqiang Cao,[1,2] Jianyang Wu,[2,3,a] Zhisen Zhang,[2] Bin Fang,[1] Li Peng,[1]
Tianshu Li,[4] Thijs J. H. Vlugt,[5] and Fulong Ning[1,a]

[1]*Faculty of Engineering, China University of Geosciences, Wuhan, Hubei 430074, China*
[2]*Department of Physics, Jiujiang Research Institute, Research Institute for Biomimetics and Soft Matter, Fujian Provincial Key Laboratory for Soft Functional Materials Research, Xiamen University, Xiamen 361005, China*
[3]*NTNU Nanomechanical Lab, Department of Structural Engineering, Norwegian University of Science and Technology (NTNU), Trondheim N-7491, Norway*
[4]*Department of Civil & Environmental Engineering, The George Washington University, Washington, DC 20052, USA*
[5]*Process and Energy Department, Delft University of Technology, Leeghwaterstraat 39, 2628CB Delft, The Netherlands*

A sound knowledge of fundamental mechanical properties of water ice is of crucial importance to address a wide range of applications in earth science, engineering, as well as ice sculpture and winter sports, such as ice skating, ice fishing, ice climbing, bobsleighs, and so on. Here, we report large-scale molecular dynamics (MD) simulations of mechanical properties of bi- and poly-crystalline hexagonal ice (I_h) under mechanical loads. Results show that bicrystals, upon tension, exhibit either brittle or ductile fracture, depending on the microstructure of grain boundaries (GBs), whereas they show ductile fracture by amorphization and crystallographic slips emitted from GBs under compression. Under shearing, the strength of bicrystals exhibits a characteristic plateau or sawtooth behavior drawn out the initial elastic strains. Nanograined polycrystals are destabilized by strain-induced amorphization and collective GB sliding. Their mechanical responses depend on the grain size. Both tensile and compressive strengths decrease as grain size decreases, showing inverse Hall-Petch weakening behavior. Large fraction of amorphous water structure in polycrystals with small grain size is mainly responsible for the inverse Hall-Petch softening. Dislocation nucleation and propagation are also identified in nanograined ice, which is in good agreement with experimental measurements. Beyond the elastic strain, a combination of GB sliding, grain rotation, amorphization and recrystallization, phase transformation, and dislocation nucleation dominate the plastic deformation in both bicrystals and polycrystals. © *2018 Author(s). All article content, except where otherwise noted, is licensed under a Creative Commons Attribution (CC BY) license (http://creativecommons.org/licenses/by/4.0/).* https://doi.org/10.1063/1.5042725

I. INTRODUCTION

Water is one of the most essential substances to life on Earth. A water molecule is composed of one oxygen atom and two hydrogen atoms, and the oxygen atom is covalently bonded to the two hydrogen atoms. The two hydrogen atoms of each water molecule can be weakly bonded to other two water molecules in hydrogen bond form, respectively. Upon cooling, water tends to freeze into ice. So far, over 15 different solid-state crystal structures of water, including ice XVI, XVII from clathrates and ice XVIII, have been identified with the aid of experimental and computational

[a]Corresponding Authors: Jianyang Wu (Email: jianyang@xmu.edu.cn), Department of Physics, Jiujiang Research Institute, Research Institute for Biomimetics and Soft Matter, Fujian Provincial Key Laboratory for Soft Functional Materials Research, Xiamen University, Xiamen 361005, China and Fulong Ning (Email: nflzx@cug.edu.cn), Faculty of Engineering, China University of Geosciences, Wuhan, Hubei 430074, China.

techniques.[1–4] Hexagonal ice (I_h) is the most common form of crystalline water on Earth,[5] and it has a hexagonal symmetry with space group of *P6₃/mmc*.[6,7] Each water molecule in I_h is surrounded tetrahedrally by four nearest neighbors centered about the molecule,[6] forming an O-O-O angle of approximately 109.5°. To date, a lot of efforts have been devoted to understanding ice nucleation mechanism and phase transformation in the past few decades.[8] Both homogeneous and heterogeneous water ice nucleation processes were identified.[9–22] Structurally, solid-state phase transformation of ice occurs under certain external settings.[23–25] Mechanical instability in the water framework during pressurization is responsible for phase transformation.

The mechanical properties of ice have also received great attention because of their scientific and engineering importance to a number of diverse aspects, e.g., the movement and breakup of glaciers, man-made architecture in cold regions, ice sculpture, winter sports (ice skating, ice fishing, ice climbing, bobsleighs), cold-ocean's exploration and transportation, global climate, to name a few.[26–30] Up to now, a large number of studies have been conducted to investigate mechanical properties of ice under various conditions via both experiments and computational simulations.[31–47] It was reported that Young's modulus of monocrystalline ice varies from 8.6 GPa to 12 GPa along different directions at a temperature near the melting point.[48,49] Using first-principles calculations, Jendi *et al.*[50] showed that Young's Modulus of I_h along the *c*-axis is 23.8 and 25.1 GPa for the Bernal-Fowler and Hayward-Reimers lattices, respectively. With regard to polycrystalline ice, its mechanical properties are greatly sensitive to both external and internal factors, e.g., measured temperature and method, structural type and grain size.[35] Young's modulus and Poisson's ratio of polycrystalline ice were found to vary from 6.0-12.0 GPa and 0.29-0.60, respectively, depending on these factors.[35] The Young's modulus of polycrystalline ice obtained from bending, extension, and compression methods ranges from 0.3 to 11 GPa, depending on the measured temperature and grain size.[51] Waite *et al.*[52] reported via pulse-transmission method that Young's modulus and the Poisson's ratio of polycrystalline ice with a grain size of around 180-250 μm at 260 K are around 9.1-9.5 GPa and 0.33 ± 0.01, respectively. By measuring dumbbell shaped molded ice specimens with an averaged grain size of approximately 0.77 mm, Hawkes *et al.*[45] obtained a tensile Young's modulus of 5.5 GPa at 266.15 K. For sea ice samples, by using the velocity of ultrasonic waves, Young's modulus was found to decrease from 10 to 6.5 GPa as the content of brine increases from 0 to 0.1 as a fraction of the total volume.[53–55] By finite element simulations (FEM), Elvin showed that the Young's modulus and Poisson ratio of polycrystalline ice without grain boundary (GB) sliding are 9.58 GPa and 0.33 at 257.15 K, respectively, while as GB sliding in polycrystals are taken into account, they are 7.83 GPa and 0.45, respectively.[56] Apart from the mechanical stiffness above, mechanical strengths of ice under both tension and compression were also studied. Upon tension, the strength of ice varies from 0.7 to 3.1 MPa, also depending on temperature, strain rates, and samples.[31,32,37–39,45,46,57] As an example, the tensile strength of polycrystalline snow ice at 255.15 K was found to be around one fifth higher than that at 273.05 K.[37] Experimental investigations by Mohamed *et al.*[58] showed that the strain rate has pronounced effects on tensile strength of ice, and ice generally fractures within the gauge section of the specimens. At a low strain rate of 10^{-3}/s, the tensile strength of polycrystals at 263.15 K is 1.4 MPa,[39] whereas at a high strain rate of around 10^7/s, it increases to 47 MPa.[59] It was also shown that the tensile strength of polycrystalline ice is grain size dependent.[31–33] The tensile strength of polycrystalline ice with grain size varying from 1.5 to 5.8 mm decreases with an increasing of grain size at 268.15 K below strain rates of 4×10^{-6}/s. This is attributed to the grain-size effect on the balance of operative deformation mechanisms.[47] However, when the strain rate exceeds the value of 4×10^{-6}/s, it increases as the grain size increases. This is explained by internal micro-fracturing and extensive deformation in GB regions.[47] Upon compression, polycrystalline ice also exhibits significant differences in strength due to external and internal factors. Haynes reported that the uniaxial compressive strength of ice at 219.15 K is approximately one order of magnitude higher than that at 273.05 K.[37] Compressive strengths of ice have positive strain-rate sensitivity in the applied strain rates within the range of 60-1400/s.[34] Moreover, polycrystalline ice was found to follow a Hall-Petch behavior in compressive strength.[60,61] The compressive strength of fresh-water, granular polycrystalline I_h increases with decreasing grain size (1 mm - 10 mm), decreasing temperature (263.15 K - 223.15 K) and decreasing strain rate (10^{-3} - 10^{-1} s^{-1}) at 263.15 K.[60] Jones and Chew[62] reported that there was no significant dependence of compressive strength of polycrystalline ice on grain size ranging from 0.6 to 2.0 mm

at 263.15 K and a strain rate of 5.5×10^{-4} s^{-1}. High values of peak stress were resulted for sample size/crystal size ratios less than 12.[62,63]

Furthermore, deformation behaviors and rheology of ice have been investigated in the past few decades.[64] By uniaxial compressive experiments on polycrystalline ice, Jacka *et al.* demonstrated that the minimum flow rate of isotropic polycrystalline ice was of little or no crystal size dependence.[65] Visible cracks have not been found in laboratory-prepared randomly-oriented ice at low strain rates.[66] Instead, Duval *et al.*[67] reported that the diffusional flow and the transient behavior in ice show grain size-dependence. More than four independent slip systems govern the compatible deformation of ice polycrystals. Both deformation of the grains and slips at the GBs were found to contribute to the deformation process of ice at temperature ranging from 233.15 to 270.15 K.[51] Muguruma[68] reported that GBs were a prominent source of dislocations in the early stage of deformation of columnar-grained ice, and the maximum stress of columnar-grained ice was grain size-dependent. Under compressive stresses ranging from around 0.1 to 1 MPa at a temperature from 263.15 K to the melting-point, a transient creep component and a continuing or quasi-viscous component have been found by Glen[69] in ice creep. In addition, ice rheology at low stress was also demonstrated to exhibit a strong dependence on the interactions between ice crystals.[70] Moreover, ice properties have also been studied *in situ* for the analysis of flow of glaciers and ice sheets.[71,72] Creep experiments on fine-grained ice[73] demonstrated that superplastic flow of ice at stresses less than 0.1 MPa governs the rate-limiting creep mechanism under a wide range of temperatures and grain sizes.

Despite many efforts made, our understanding on mechanical properties of ice still remains very limited, particularly, on the deformation mechanisms, strain-induced structural transition and dislocations at the molecular level. As the Hall-Petch relationship is established experimentally in polycrystalline ice with millimeter-sized grains, it is interesting to understand whether this Hall-Petch strengthening behavior is expected to continue or switch to an inverse Hall-Petch softening in nanograined ice (grain size ranging from 1 to 100 nm). However, experimental investigation is challenging because of the difficulties in preparing high-quality nanograined samples and experimental nano-visualizing of structure of GBs and deformation responses. Classic molecular dynamics (MD) simulations as an important tool have been successfully applied to understand formation mechanisms, thermodynamic and mechanical properties of a variety of solid-state materials at the molecular level.[9,16,74,75] This study provides critical knowledge of mechanical properties of bi- and poly-crystalline I$_h$ under mechanical loadings. The failures and plastic deformation mechanisms, such as GB sliding, GB accommodation mechanisms and intragranular deformation, are elucidated by classic MD simulations at nanoscale (1 - 100 nm). These results are of key importance in glacier studies, ice engineering, and frozen ground mechanics and operations in polar area. Moreover, this work provides the molecular insight to understand the differences in mechanical mechanisms of ice, clathrate hydrate and ice-like water-dominant materials that often coexist with ice in the permafrost regions.

II. MODEL AND METHODS

A. Atomic models

The initial atomic structure of monocrystalline I$_h$ was obtained by X-ray diffraction results.[76] One unit cell of monocrystalline I$_h$ is composed of 16 water molecules. Figures 1a–1c present three geometrical configurations of I$_h$ with different crystal planes highlighted by green. Monocrystalline I$_h$ shows hexagonal plates and columns with top and bottom faces those are basal planes {0001}, and 6-equivalent side faces which are called the prism faces a. Additionally, planes in I$_h$ formed by the sides of the chair-like structure are the secondary prism faces {11$\bar{2}$0}. Because of the complexity of GB structures in polycrystals, three distinct bicrystals formed by two different single crystals were specifically created to reveal the mechanical characteristics of GBs under tensile, compressive and shearing loads. Figure 1f presents a typical side-viewed relaxed bicrystalline structure with a flat and cohesive GB that is formed by joining two monocrystals with {11$\bar{2}$0} and {0001} planes. Five- and seven-membered rings identified at GB were green- and yellow-highlighted, respectively.
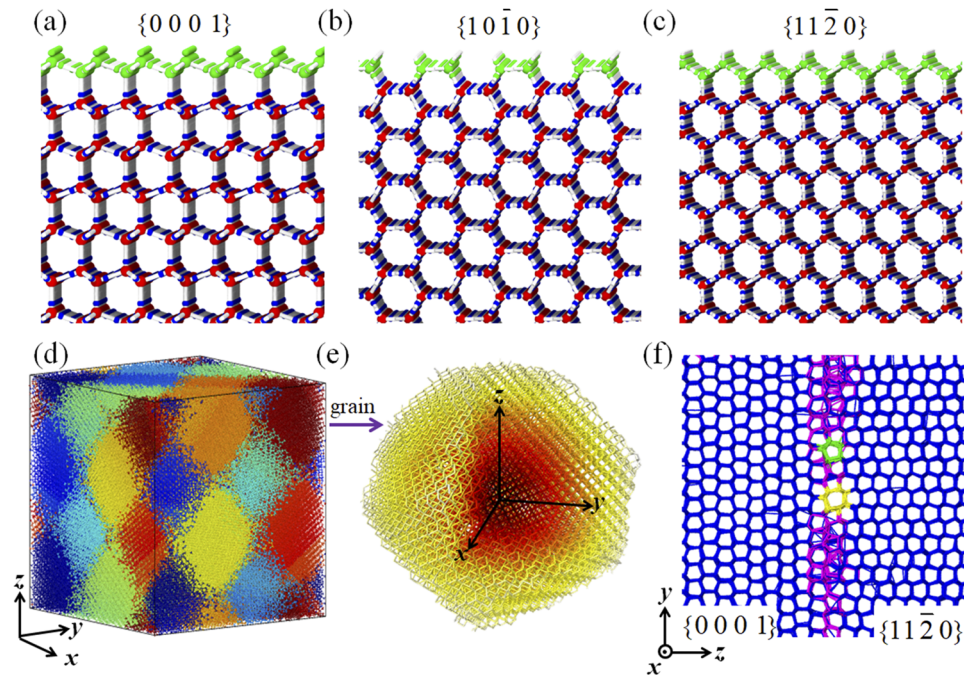
FIG. 1. Molecular models of I_h. (a)-(c) Molecular structures of monocrystalline I_h with specific crystal plane colored by green. The oxygen atoms and hydrogen atoms in the interior are rendered by red and blue, respectively. (d) Three-dimensional relaxed polycrystals of I_h with an average grain size of 15.87 nm. To clearly demonstrate the polycrystalline structure, neighboring grains are rendered by different colors. (e) One typical ice grain with the geometry of the body-centered cubic Wigner-Seitz cell from the polycrystals. (f) A bicrystal with a flatly cohesive GB formed by joining two monocrystals with $\{11\bar{2}0\}$ and $\{0001\}$ planes. For a clarification of the microstructures, identified five- and seven-membered rings of water at the flat GB are colored by green and yellow, while other interfacial and interior water molecules are rendered by pink and blue, respectively.

To reveal the effect of grain size on mechanical properties of polycrystalline I_h, five samples containing a number of monocrystalline grains with average grain sizes ranging from 4.54 to 15.87 nm were constructed based on a Voronoi construction.[77,78] All polycrystals had identical dimensions of $40 \times 40 \times 40$ nm^3. The number of grains determined by grain size in polycrystals ranged from 16 to 686. The average grain size in polycrystals is defined as follows:

$$d = \sqrt[3]{\frac{L^3}{N}}. \tag{1}$$

where L and N are the length of samples (nm) and the number of grains in polycrystals, respectively. Figure 1d shows a representative three-dimensional (3D) molecular configuration of polycrystalline I_h with an average grain size of 15.87 nm, and each grain is colored for clarification. The orientations of grains in polycrystals are randomly distributed. Figure 1e displays one typical grain with a geometry of the body-centered cubic Wigner-Seitz cell from the polycrystal. To avoid artificial particle overlaps in the polycrystals, molecules that are closer than 0.1 nm to any adjacent one in the neighboring grains were removed. To facilitate further statistical analysis, four polycrystalline samples with identical average grain size but different GBs were generated. Each polycrystal was composed of approximately 1,930,000 water molecules.

B. Forcefields

A mono-atomic model was adopted to describe water molecules. The tetrahedral short-ranged interactions among mono-atomic water are modeled by the available Stillinger-Weber (SW) model.[79] This coarse-grained water model[80,81] is over 2 orders of magnitude more computationally efficient than a fully atomistic model in reproducing a range of properties of liquid and solid phases of water.[80] Moreover, this model was successfully applied to investigate the mechanical properties of methane

hydrate.[82] All molecular models of bi- and poly-crystals were based on coarse-grained mW water model.

C. Mechanical MD tests

Prior to MD calculations of uniaxial straining, all molecular structures were quasi-statically relaxed to a local minimum energy configuration by the conjugate gradient method with an energy tolerance of 1.0×0^{-4} eV and a force tolerance of 1.0×10^{-4} eV/Å.[83] MD relaxations were conducted with 1.0×10^{6} timesteps at 223.15 K and atmospheric pressure in the NPT (constant number of particles, constant pressure, and constant temperature) ensemble, and then with another 1.0×10^{6} timesteps at 223.15 K under NVT (constant number of particles, constant volume, and constant temperature) ensemble. The Nosé-Hoover thermostat and barostat method with damping times of 0.1 and 0.5 ps were used to control the temperature and pressure, respectively. Our MD calculations allowed ice structures to relax in order to obtain the stable structures. The velocity-Verlet integration algorithm was employed to integrate the equations with timestep of 1 fs. 3D periodic boundary conditions were applied in three directions to obtain data. Initial velocities of water particles in the systems were assigned following a uniform distribution according to the given temperature. In this study, the tensile (compressive) strain is defined as

$$\varepsilon = \frac{|l - l_0|}{l_0} = \frac{\Delta l}{l_0} \qquad (2)$$

where l_0 and l are the original length and the final length of ice sample along the deformational direction, respectively.

For mechanical tests, the uniaxial loadings were conducted by the deformation control technique in the NpT ensemble. This procedure was carried out on the relaxed samples with a constant strain rate of 1.0×10^{8} s^{-1} by uniformly rescaling the z-coordinates of all molecules every 1000 timesteps. Deformational MD simulations were performed in a modified NpT ensemble, specifically, NVT in the loading direction but NpT in the lateral directions. The deformational MD simulations were performed in N$L_z p_x p_y$T ensemble, where L_z is the length of simulation box along the loading direction. The Nosé–Hoover anisotropic barostat and thermostat was employed in N$L_z p_x p_y$T ensemble to control pressure only in the lateral directions independently and temperature. This allowed ice samples to experience expansion/contraction in transverse directions due to the Poisson's effect. The stress of water particle was calculated based on the virial definition of stress using forces on the particles collected during MD simulations. Both stress and potential energy of molecules in systems were averaged over 5000 timesteps to eliminate thermal oscillations. All MD calculations were performed by using the Large-scale Atomic-Molecular Massively Parallel Simulator (LAMMPS) software package.[84]

To identify and visualize dislocations and stacking faults of hexagonal structures during MD simulations, an extended common neighbor analysis (CNA) method[85] was employed. The extended CNA is able to classify pairs of particles based on their local environments. Furthermore, the topology of water rings in GBs was also identified by using the "shortest path ring" algorithm developed by Franzblau.[86] The development of dislocation activities during deformation was also observed. The dislocation results were obtained by means of the Dislocation Extraction Algorithm (DXA) method.[87]

D. Mechanical properties of bicrystals

1. Mechanical properties of bicrystals under both tension and compression

Mechanical properties of bicrystalline I_h with three distinct GB structures under both tension and compression are examined. Figure 2a shows the simulated stress-strain curves of bicrystals with typical $\{11\bar{2}0\}|\{00\,0\,1\}$, $\{11\bar{2}0\}|\{01\bar{1}0\}$ and $\{00\,0\,1\}|\{01\bar{1}0\}$ GB structures subjected to tension along the directions perpendicular to GBs. Bicrystals show initially a linear response, followed by a nonlinear elastic response. However, differences in their peak tensile strengths are detected. The peak tensile strength from the highest to the lowest are sorted as $\{11\bar{2}0\}|\{01\bar{1}0\} > \{11\bar{2}0\}|\{00\,0\,1\} > \{00\,0\,1\}|\{01\bar{1}0\}$, which indicates different cohesive energy of those GB structures. For bicrystals with $\{11\bar{2}0\}|\{00\,0\,1\}$ and $\{00\,0\,1\}|\{01\bar{1}0\}$ GB structures, tensile stresses almost drop to zero after the peak strength, suggesting a brittle fracture mechanism. For the one with $\{11\bar{2}0\}|\{01\bar{1}0\}$ GB structure, however, it shows a ductile fracture pattern as indicated by Figure 2a. Tensile stresses oscillate
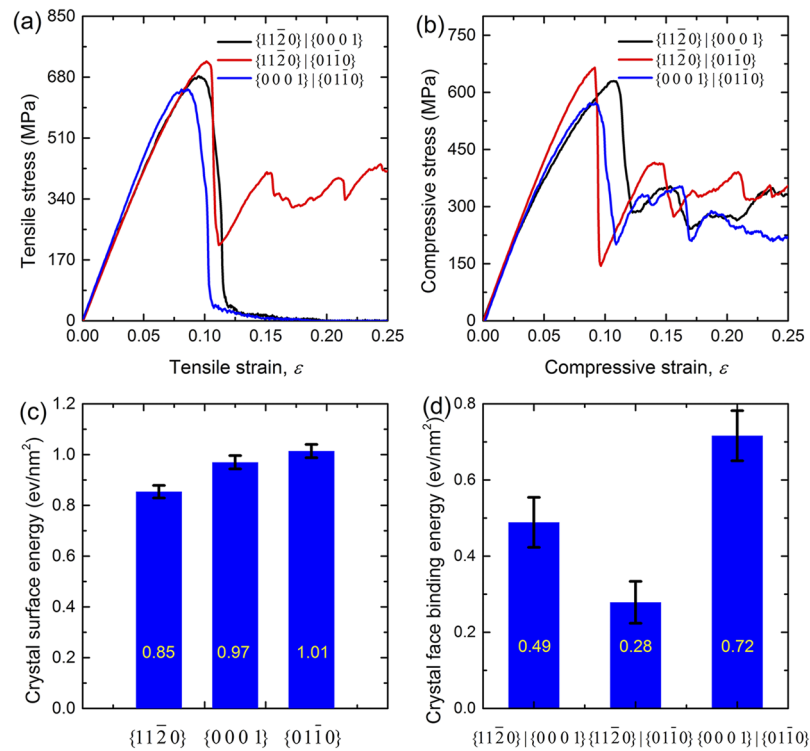
FIG. 2. Mechanical tensile and compressive responses of bicrystalline I_h. (a)-(b) The stress-strain diagrams of bicrystals under tension and compression, respectively. (c) The histograms of crystal surface energy of I_h. (d) The histograms of crystal face binding energy of bicrystals.

at around 340 MPa after the sudden drop of stress. The fracture strains are also found sensitive to bicrystalline structures. Upon compression, as shown in Figure 2b, the mechanical response is similar to the case of bicrystal with $\{11\bar{2}0\}|\{01\bar{1}0\}$ GB structure under tension. The order of peak compressive strength is found identical to that of peak tensile strength. To understand the differences in ultimate mechanical strength, the energy of selected crystal surface that forms the GB structures and GB binding energy are accordingly calculated, as presented in Figures 2c and d. Apparently, the $\{11\bar{2}0\}$ plane has the lowest energy, while the $\{01\bar{1}0\}$ plane shows the highest energy. For binding energy of GBs, their order is found to be $\{00\,0\,1\}|\{01\bar{1}0\} > \{11\bar{2}0\}|\{00\,0\,1\} > \{11\bar{2}0\}|\{01\bar{1}0\}$, which is consistent with the calculated ultimate mechanical strengths. In addition, the Young's moduli of the bicrystal determined from initial slopes of stress-strain curves are around 7.6-9.1 GPa.

To unravel tensile and compressive deformation mechanisms, a number of typically localized snapshots of bicrytalline I_h are captured and shown in Figure 3. By examining the microstructures of bicrystals at equilibrium state (zero-strain), it is observed that all water molecules in GBs are identified and GB structures have comparable potential energy to the bulk counterparts, indicating highly cohesive GB structures. Moreover, structural defects,[88] including five- and seven-membered rings that commonly exist in graphene and diamond, are observed in GBs. These defects also explain the superior stiffness and mechanical strength of bicrystals. When the tensile strain exceeds the critical values, molecular structures of bicrystals with $\{11\bar{2}0\}|\{00\,0\,1\}$ and $\{00\,0\,1\}|\{01\bar{1}0\}$ GBs destabilize, as demonstrated by Figures 3a-3, a-7, c-3 and c-7. This corresponds to a sharp drop of stress in stress-strain curves of Figure 2a. Further strain causes the complete decohesion of GBs, suggesting brittle fracture mechanism. For a bicrystal with $\{11\bar{2}0\}|\{01\bar{1}0\}$ GB, however, a ductile fracture mechanism is observed, as illustrated by Figure 3b. This plastic deformation mechanism differs from those of monocrystal.[82] The bicrystal destabilizes by crystallographic slip along the $(11\bar{2}0)$ crystal plane that emits from one site of the pre-existed GB. This results in the formation of a new GB that is less cohesive than pre-existed GB. As a result of its small cohesive force, the following plastic deformation is controlled by sliding of this new GB accompanied by recrystallization and dislocation
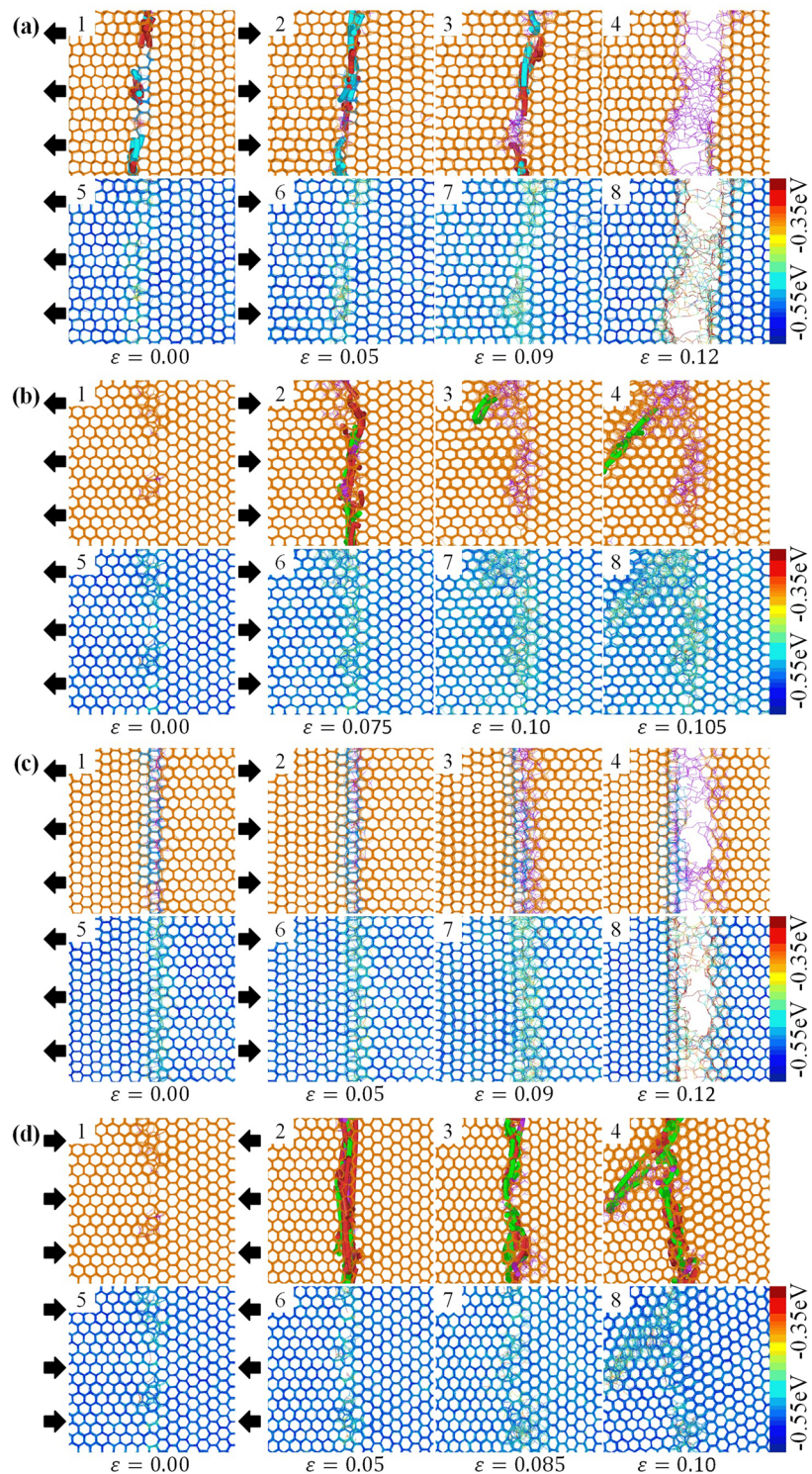
FIG. 3. Snapshots of different bicrystalline I_h near GB. (a)-(c) Molecular snapshots of bicrystals with $\{11\bar{2}0\}|\{00\,0\,1\}$, $\{11\bar{2}0\}|\{01\bar{1}0\}$ and $\{00\,0\,1\}|\{01\bar{1}0\}$ GB structures under tension at different strains, respectively. (d) Molecular snapshots of bicrystals with $\{11\bar{2}0\}|\{01\bar{1}0\}$ GB structures under compression at different strains. Water molecules in snapshots #1-4 are colored according to the identified type of structural phase; Hexagonal, cubic and unidentified water structures are rendered by orange, light blue and purple for clarification, respectively. Strain-induced dislocations in bicrystals are illustrated by solid segments. Different colored segments represent different types of dislocations; $1/3\langle 1\,\bar{2}\,1\,0\rangle$, $\langle 0\,0\,0\,1\rangle$, $\langle 1\,\bar{1}\,0\,0\rangle$, $1/3\langle 1\,\bar{1}\,0\,0\rangle$, and unidentified dislocations are rendered by green, yellow, pink, sky-blue and red for clarification, respectively. Water molecules in snapshots #5-8 are rendered according to their potential energy.

at GBs. The two distinct fracture patterns are mainly attributed to the difference in crystal face binding energy. Upon compression, all bicrystals show ductile fracture behaviors. As shown in Figure 3d, the plastic deformation mechanism is similar to that of bicrystal with {11$\bar{2}$0}|{01$\bar{1}$0} GB structures under tension.

2. Mechanical properties of bicrystals under shear strain

Shearing responses of bicrystals are also key mechanical properties of interest in solid-state materials. It is instructive to examine mechanical properties of bicrystalline I_h under pure shear deformation in GBs planes. Pressures in the directions that are perpendicular to shear directions are controlled to be ambient pressure during the shear deformations. Figure 4 shows the simulated shear mechanical properties of bicrystals with different GBs along two nonequivalent shear directions. Obviously, the features of all shearing curves differ from those of tensile and compressive ones. By comparing MD shearing results of bicrystals, bicrystals with {11$\bar{2}$0}|{00 0 1} and {00 0 1}|{01$\bar{1}$0} GBs show very limited elasticity and small first peak shear strengths, indicating their least cohesive forces of GBs. In sharp contrast, for bicrystal with {11$\bar{2}$0}|{01$\bar{1}$0} GB, the similarity between elastic shear, tension and compression strains and its large first peak shear strengths indicate the large cohesive forces of {11$\bar{2}$0}|{01$\bar{1}$0} GB. Those agree with the results of tensile and compressive MD simulations. Beyond yield points, three distinct categories of shear stress-strain behaviors are classified, depending on bicrystalline structures and shearing directions. Upon $\frac{(1\,1\,\bar{2}\,0)[0\,0\,0\,1]}{(0\,0\,0\,1)[1\,1\,\bar{2}\,0]}$ directional shear load, bicrystal with {11$\bar{2}$0}|{00 0 1} GB shows significant strain hardenings, e.g., shear strength increases from 70 to 165 MPa as the strain increases from 0.1 to 0.22 (Figure 4a).
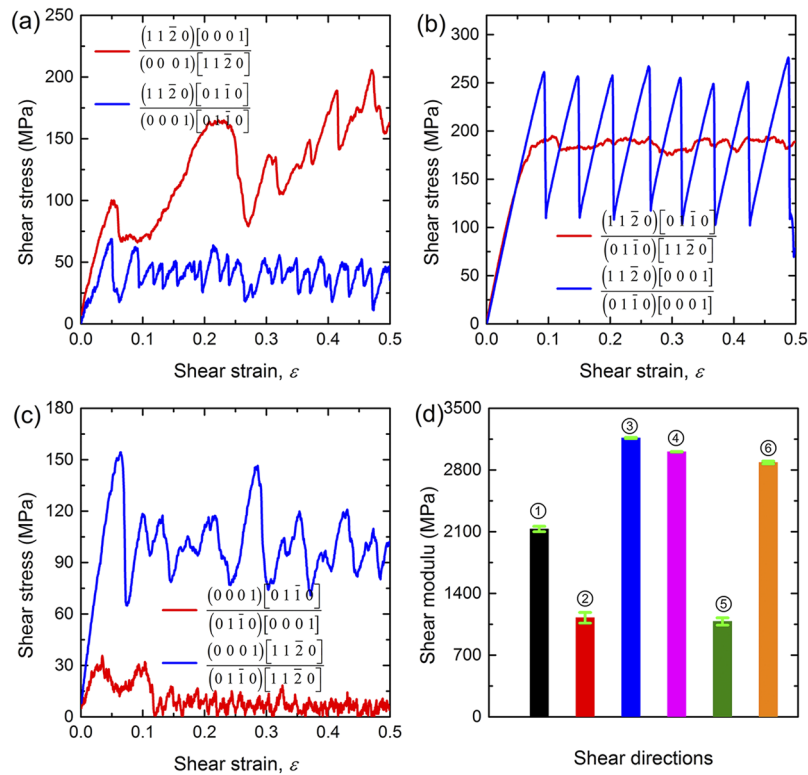

FIG. 4. Mechanical shear responses of bicrystalline I_h. (a)-(c) The stress-strain diagrams of bicrystals with {11$\bar{2}$0}|{00 0 1}, {11$\bar{2}$0}|{01$\bar{1}$0} and {00 0 1}|{01$\bar{1}$0} GB structures under two nonequivalent directional shear deformations, respectively. (d) The shear modulus histograms of bicrystals along the corresponding two shearing directions. ①-⑥ represent the shearing directions in $\frac{(1\,1\,\bar{2}\,0)[0\,0\,0\,1]}{(0\,0\,0\,1)[1\,1\,\bar{2}\,0]}$, $\frac{(1\,1\,\bar{2}\,0)[0\,1\,\bar{1}\,0]}{(0\,0\,0\,1)[0\,1\,\bar{1}\,0]}$, $\frac{(1\,1\,\bar{2}\,0)[0\,1\,\bar{1}\,0]}{(0\,1\,\bar{1}\,0)[1\,1\,\bar{2}\,0]}$, $\frac{(1\,1\,\bar{2}\,0)[0\,0\,0\,1]}{(0\,1\,\bar{1}\,0)[0\,0\,0\,1]}$, $\frac{(0\,0\,0\,1)[0\,1\,\bar{1}\,0]}{(0\,1\,\bar{1}\,0)[0\,0\,0\,1]}$ and $\frac{(0\,0\,0\,1)[1\,1\,\bar{2}\,0]}{(0\,1\,\bar{1}\,0)[1\,1\,\bar{2}\,0]}$, respectively.

This indicates formation of new structure during shearing deformation. Upon $\frac{(1\,1\,\bar{2}\,0)[0\,1\,\bar{1}\,0]}{(0\,0\,0\,1)[0\,1\,\bar{1}\,0]}$ shearing, however, steady oscillations in shear strength at around 40 MPa with amplitude of around 10 MPa are detected during the entire shear deformation. This suggests that the bicrystal undergoes a series of repeating processes of local shear strain and local shear stress relaxation, indicating plastic deformation behavior. Such oscillations in shear strength are also detected in other two bicrystals subjected to $\frac{(1\,1\,\bar{2}\,0)[0\,0\,0\,1]}{(0\,1\,\bar{1}\,0)[0\,0\,0\,1]}$ and $\frac{(0\,0\,0\,1)[1\,1\,\bar{2}\,0]}{(0\,1\,\bar{1}\,0)[1\,1\,\bar{2}\,0]}$ shear strains. This interesting feature is similar to a sawtooth-like oscillation observed in the unfolding of bio-macromolecules and coiled carbon nanotubes (CNTs).[89–92] Particularly, a perfect sawtooth-fluctuation of shear strength in bicrystal with {11$\bar{2}$0}|{01$\bar{1}$0} GB under $\frac{(1\,1\,\bar{2}\,0)[0\,0\,0\,1]}{(0\,1\,\bar{1}\,0)[0\,0\,0\,1]}$ shear deformation is identified (Figure 4b). With regard to bicrystals with {11$\bar{2}$0}|{01$\bar{1}$0} and {00 0 1}|{01$\bar{1}$0} GBs under the other shear loads, plateau stages with nearly constant shear stress to large strain are revealed. However, their plateau stresses strikingly differ by over one order of magnitude (Figure 4b–c). This explains their distinct shear mechanical characteristics of GB structures. Shear moduli of those bicrystals extracted from the initial slopes of shear response curves are plotted in Figure 4d. Shear stiffness ranging from 1.1 to 3.1 GPa is over one order of magnitude lower than the tensile and compressive stiffness. Bicrystal with {11$\bar{2}$0}|{01$\bar{1}$0} GB structure exhibits large shear modulus (around 3.1 GPa) and negligible difference in shear modulus is found for the two nonequivalent shearing directions. However, the shear moduli of bicrystals with {11$\bar{2}$0}|{00 0 1} and {00 0 1}|{01$\bar{1}$0} GBs show strong loading-directional dependence. For example, as shown in Figure 4d, the shear modulus of bicrystal with {00 0 1}|{01$\bar{1}$0} GB under $\frac{(0\,0\,0\,1)[1\,1\,\bar{2}\,0]}{(0\,1\,\bar{1}\,0)[1\,1\,\bar{2}\,0]}$ directional shear load is over twice of that under $\frac{(0\,0\,0\,1)[0\,1\,\bar{1}\,0]}{(0\,1\,\bar{1}\,0)[0\,0\,0\,1]}$ one.

To elucidate the shear deformation mechanism of bicrystalline I_h, the associated molecular deformation modes are analyzed by examining the microstructural evolution during shearing process. Figure 5 shows the microstructures of bicrystals with different GBs along the two nonequivalent directions at different shear strains. For bicrystal with {11$\bar{2}$0}|{00 0 1} GB subjected to shear strain along the $\frac{(1\,1\,\bar{2}\,0)[0\,0\,0\,1]}{(0\,0\,0\,1)[1\,1\,\bar{2}\,0]}$ direction, as shown in Figure 5a, 1/3⟨1 $\bar{1}$ 0 0⟩ and unidentified dislocations accompanied with phase transformation from stable hexagonal to metastable cubic phase dominate the plastic deformation. Shear strain-induced large-scale structural transition initiates from the GB and only develops in one joined monocrystal with {11$\bar{2}$0} plane, resulting in strain-hardening behavior as observed in Figure 4a. Moreover, mechanical strain-induced phase transition is different from previous observations that metastable cubic ice (I_c) transforms into stable I_h by heating.[93–96] With regard to the case under $\frac{(1\,1\,\bar{2}\,0)[0\,1\,\bar{1}\,0]}{(0\,0\,0\,1)[0\,1\,\bar{1}\,0]}$ directional shearing, GB sliding accompanied by 1/3⟨1 $\bar{1}$ 0 0⟩ and unidentified dislocations occurring at GB governs plastic deformation, as indicated by Figure 5b. When $\frac{(1\,1\,\bar{2}\,0)[0\,1\,\bar{1}\,0]}{(0\,1\,\bar{1}\,0)[1\,1\,\bar{2}\,0]}$ directional shear strain is applied to bicrystal with {11$\bar{2}$0}|{01$\bar{1}$0} GB, GB sliding accompanied by bond breaking at GB occurs as shear strain reaches around 0.09. Beyond this critical shear strain, a series of repeated formation and destruction of massively stable five- and seven-membered rings at GB (Figures 5c-4 and -6) are responsible for the nearly constant large shear strength. Formation and destruction of five- and seven-membered defect pair was also identified as the controlling step in homogeneous ice melting,[88,97,98] similar to other solid materials.[99] It is also found in the nucleation and growth of ice,[100] and the large-angle grain boundary is found to form spontaneously within a 45-degree wedge. A small number of 1/3⟨1 $\bar{2}$ 1 0⟩ dislocations were found in this plastic deformation. For the $\frac{(1\,1\,\bar{2}\,0)[0\,0\,0\,1]}{(0\,1\,\bar{1}\,0)[0\,0\,0\,1]}$ directional load that is perpendicular to planar five- and seven-membered rings at GBs. However, repeated process of reformation and destruction of strongly cohesive GB results in the perfect sawtooth-fluctuation of shear strength. These results indicate strong anisotropy in shear responses of GBs that is composed of pentagonal, hexagonal and heptagonal water structures. 1/3⟨1 $\bar{2}$ 1 0⟩ dislocation also intermittently occurs during the plastic deformation (Figure 5d). For bicrystals with {00 0 1}|{01$\bar{1}$0} GB structure that mainly consists of
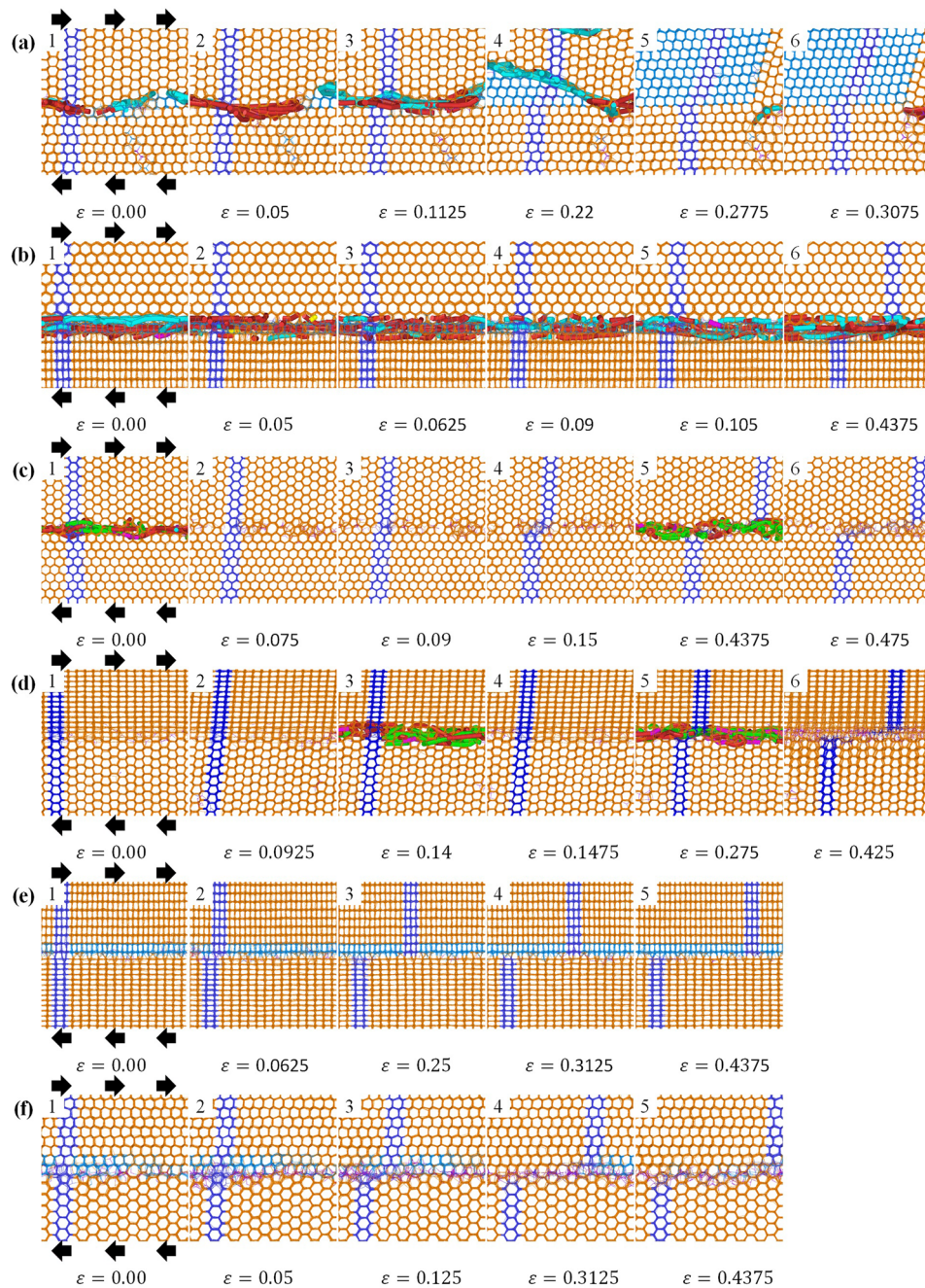
FIG. 5. Snapshots of bicrystalline I_h under shear deformation along different directions. (a)-(f) Molecular snapshots of bicrystals subjected to $\frac{(1\,1\,\bar{2}\,0)[0\,0\,0\,1]}{(0\,0\,0\,1)[1\,1\,\bar{2}\,0]}$, $\frac{(1\,1\,\bar{2}\,0)[0\,1\,\bar{1}\,0]}{(0\,0\,0\,1)[0\,1\,\bar{1}\,0]}$, $\frac{(1\,1\,\bar{2}\,0)[0\,1\,\bar{1}\,0]}{(0\,1\,\bar{1}\,0)[1\,1\,\bar{2}\,0]}$, $\frac{(1\,1\,\bar{2}\,0)[0\,0\,0\,1]}{(0\,1\,\bar{1}\,0)[0\,0\,0\,1]}$, $\frac{(0\,0\,0\,1)[0\,1\,\bar{1}\,0]}{(0\,1\,\bar{1}\,0)[0\,0\,0\,1]}$ and $\frac{(0\,0\,0\,1)[1\,1\,\bar{2}\,0]}{(0\,1\,\bar{1}\,0)[1\,1\,\bar{2}\,0]}$ shear loadings at different strains, respectively. Black arrows indicate the shear loading directions. Water particles are colored according to the identified type of structural phase; Hexagonal, cubic and unidentified water structures are rendered by orange, light blue and purple for clarification, respectively. Specifically, uniformly selected water particles are colored by blue to clearly monitor structural changes during shearing. Strain-induced dislocations in I_h are illustrated by solid segments. Different colored segments represent different type of dislocation; $1/3\langle 1\,\bar{2}\,1\,0\rangle$, $\langle 0\,0\,0\,1\rangle$, $\langle 1\,\bar{1}\,0\,0\rangle$, $1/3\langle 1\,\bar{1}\,0\,0\rangle$ and unidentified dislocations are rendered by green, yellow, pink, sky-blue and red for clarification, respectively.

metastable cubic structure, shear deformations along the $\frac{(0\,0\,0\,1)[0\,1\,\bar{1}\,0]}{(0\,1\,\bar{1}\,0)[0\,0\,0\,1]}$ and $\frac{(0\,0\,0\,1)[1\,1\,\bar{2}\,0]}{(0\,1\,\bar{1}\,0)[1\,1\,\bar{2}\,0]}$ directions easily break metastable hydrogen bonds, resulting in early GB sliding. Instead, dislocation-free region is found during the entire deformation process (Figure 5e–f). In short, both elasticity and

plasticity in bicrystals strongly depend on microstructures of GBs and shearing directions. Mechanical plastic deformation of bicrystals under two nonequivalent shear directions involves GB sliding, the competition mechanism among decomposition, recrystallization, and dislocations.

E. Mechanical properties of polycrystals

For conventional polycrystalline solid materials such as metals, carbon materials and methane hydrates, grain size plays a key role in their mechanical behaviors. In natural and laboratory settings, I_h was commonly observed to be grown well with polycrystalline texture. MD simulations of polycrystalline I_h with grain size varying from 4.54-15.87 nm under both tension and compression are performed to investigate mechanical properties. Figure 6a shows the initial and MD relaxed molecular structures of polycrystals with two different grain sizes. It is found from snapshots of #1 and 2 that, after MD relaxations, GBs are able to maintain their flat plane. However, besides hexagonal and amorphous structures, a cubic phase of ice structures is observed at GBs. As shown in snapshots of #3 and 4 of Figure 6a, GBs exhibit higher potential energy than that of the grain interior, indicating their metastability. By analyzing water topological rings at GBs, various structural defects containing four-, five- and seven-membered rings are found, as presented in Figure 6b.

A series of uniaxial tensile and compressive loadings on polycrystalline I_h at 223.15 K and ambient pressure were carried out. Figures 7a and b show the MD simulated mechanical stress-strain curves of polycrystals with fine grain size ranging from 4.54-15.87 nm under both tension and compression, respectively. Apparently, all polycrystals show unique mechanical responses that strikingly differ from those of bicrystalline counterparts. Particularly, characteristic features of nonlinear stress-strain curves are remarkably sensitive to the grain size under both tension and compression. Three deformational stages can be roughly observed. At the first stage, all polycrystals in all tests show linear loading responses, corresponding to the initially limited elastic deformations. Young's modulus obtained by fitting the stress-strain curves in this stage varies from 4.9 to 7.7 GPa with grain size ranging from 4.54 to 15.87 nm. The values of elastic moduli are lower than those of bicrystals in our simulations, as well as those of experimental measurements.[101,102] This is mainly attributed to differences in microstructure of samples. For example, bicrystals show infinite long GBs, while polycrystals show finite long GBs and complex triple GB junctions. Crystalline grains of ice in laboratory, engineering or nature are typically millimeter- and micron-sized,[31,47,62,65,103,104] which are orders of magnitude larger than these of polycrystalline ice in the present study. Similar reduction characteristics have been also identified in metals, diamond and methane hydrates.[82,105,106] This indicates that the quality of ice can be dictated by the grain size dependent mechanical stiffness, which indicates its useful applications in winter sports such as ice skating, ice fishing, ice climbing, and bobsleighs. Moreover, in experimental measurements, the used strain rates ranging from 10^{-7} to 10^{-2} s^{-1} [31,47,103,104] were
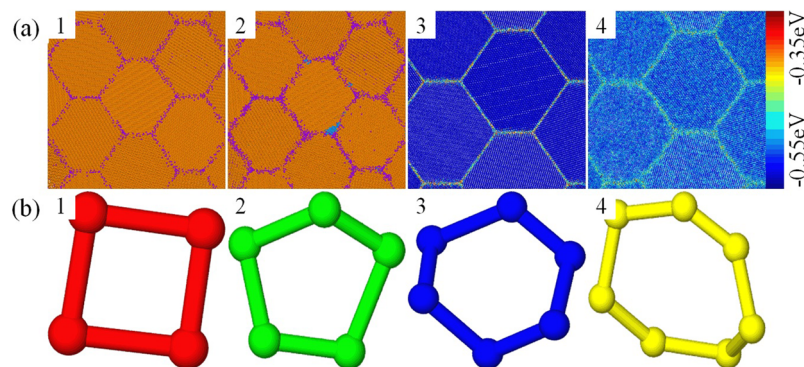

FIG. 6. Typical MD models of polycrystals. (a) Cross-sectional snapshots of polycrystals with grain sizes of 7.94 and 15.87 nm. Snapshots #1-2 show the micro-morphologies of polycrystals with grain size of 7.94 nm before and after MD relaxation, respectively, where the water molecules are colored according to their structural phases; Hexagonal, cubic and unidentified water structures are rendered by orange, light blue and purple, respectively. Snapshots #3-4 are the molecular structures of polycrystal with grain size of 15.87 nm before and after MD relaxation, respectively, where the water molecules are colored according to their potential energy. (b) Various polygonal water rings are identified at the GBs of ice polycrystals.
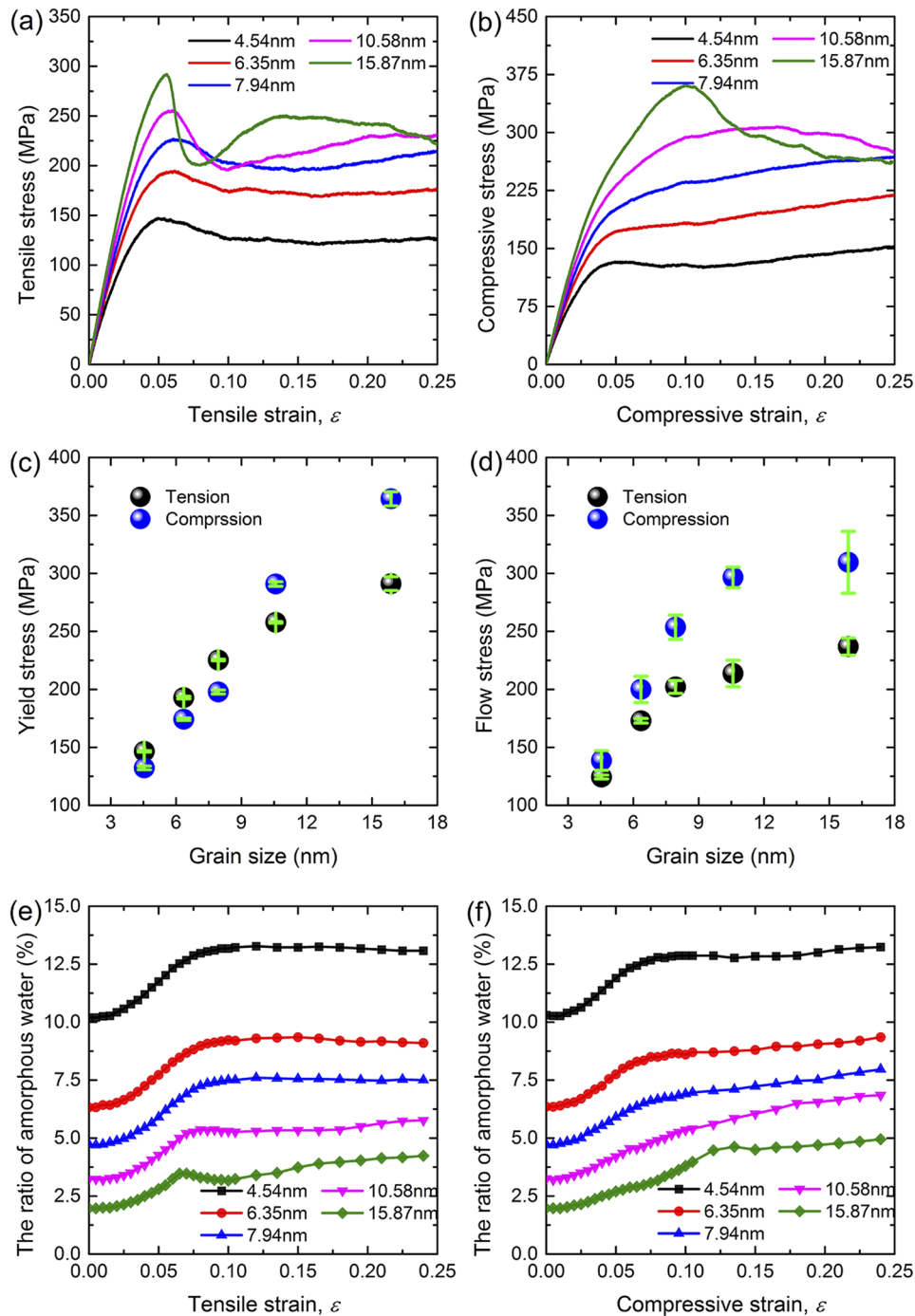
FIG. 7. Mechanical responses of polycrystalline I_h. (a)-(b) The mechanical stress-strain diagrams of polycrystals with grain size ranging from 4.54 to 15.87 nm under tension and compression, respectively. (c) Relationships between the yield strength and grain size under both tension and compression. (d) The flow stress as a function of grain size under both tension and compression. (e)-(f) Variations in the fraction of amorphous water molecules identified in polycrystals with the imposed tensile and compressive strains, respectively.

lower than that of our MD studies. The strain rates in our MD simulations may be comparable to hail stone impacts or winter sports. The second deformation stage corresponds to nonlinear mechanical responses prior to the yield points. In this stage, mechanical strength strongly depends on grain size, although all polycrystals show monotonic increasing strength, which is indicative of different

deformation elastoplasticity in polycrystal with different grain size beyond the early small elastic deformations. In addition, both yield tensile and compressive strengths are also greatly grain size-dependent, as presented in Figure 7c. Intriguingly, under tension and compression, polycrystalline I_h exhibits inverse Hall-Petch behavior. The yield stress monotonically increases as the fine grain size increases from 4.54 to 15.87 nm. Experimentally, strong dependence of mechanical strength on grain size in macroscopically grain-textured polycrystalline ice was also observed at various measurement conditions.[31,47,62,63,103,104] For example, it was reported that polycrystalline ice with millimeter-scale grains of 1.5-5.8 mm are able to follow either Hall-Petch or inverse Hall-Petch behavior, depending on the measured strain rates.[47] Currier *et al.*[31] showed that, under tensile experiments with strain rate of 1.0×10^{-6} s^{-1} at 263.15 K, the fracture strength of millimeter-sized grained ice reduces as the grain size is increased. However, Cole *et al.*[47] reported that the peak stress increases with increasing grain sizes when the applied strain rate is less than a critical value of around 4.0×10^{-6} s^{-1}. The conflicting findings from different experimental measurements suggest that deformation mechanisms of polycrystals with large grain size are sensitive to strain rate. This is indeed generally accepted in glaciology,[107] where dislocation creep is assumed to be the dominant mechanism in glaciers and ice sheets, but grain-size sensitive flow can occur at small grain sizes or at very slow strain rates.[73,107] Although the experimentally observed inverse Hall-Petch relation is in accordance with our findings, the applied strain rates are different between experiments and our MD simulations. Moreover, opposite observations between experiments (Hall-Petch) and our calculations (inverse Hall-Petch) can be mainly attributed to disparity in grain size. Previous reports via experiments or computer simulations showed very small critical grain sizes at the transition between Hall-Petch and inverse Hall-Petch relationships in metals, metallic alloys and methane hydrates.[82,108,109] It is therefore expected that the mechanical strength of extremely fine nanograined ice follows inverse Hall-Petch relationship as predicted by our simulations. For the last stage that corresponds to the deformation responses after the yield points, it is observed that the mechanical characteristics of nanograined ice are also strongly grain size dependent. Under tension, all polycrystals show strain-induced softening behavior, which becomes more pronounced for ice with larger grain size. Such strain softening is commonly observed in glassy organic materials.[110–112] The deformation responses are associated with changes in microstructures. Posterior to strain-softening, ice with grain size of 4.54 and 6.35 nm exhibits evidently steady flow stress, whereas that with grain size of 7.94 nm exhibits monotonic strain-hardening drawn out the first at strain of 0.15. Particularly, tensile strengths in polycrystals with two large grains increase, and then decline with increasing strain, reflecting a transition from strain-hardening to strain-softening, consistent with the previous experimental data.[67] Upon compression, loading responses of polycrystal with the smallest grain are similar to the case under tension. Polycrystals with grain size of 6.35 and 7.94 nm exhibit monotonic strain hardening that continues over the predefined strain of 0.25. Such strain hardening persists to a large degree relative to most metals and ceramics at high temperatures. In contrast, polycrystals with large grains display ultimate compressive strengths at critical strains followed by apparent strain-softening behavior. Figure 7d shows the average flow stress as a function of grain size. Similar to yield stress, the average flow stress increases as the grain size increases, which indicates inverse Hall-Petch behavior. Beyond ice, natural gas hydrates occurring in deep-sea sediments or permafrost regions are also icy crystalline substances. Figure 10 shows a comparison between ice and methane hydrates,[31,47,82,113–117] and both solids exhibit grain size and temperature dependent mechanical properties. However, differences can be also identified, attributed to the difference in the intrinsic water-dominated framework structure.

For some solid materials (metals, black phosphorus and methane hydrates), a large fraction of disorder molecules at GBs of polycrystals with extremely fine grains is responsible for the inverse Hall-Petch softening behavior.[82,105,118,119] Accordingly, variations of the fraction of amorphous water in polycrystals with imposed tensile and compressive strains are calculated and plotted in Figures 7e and f, respectively. At equilibrated state (zero strain), polycrystal with small grain size shows the largest fraction of disorder water particles. The existence of amorphous water molecules in GBs weakens polycrystals as indicated by the difference in mechanical properties between bicrystals and polycrystals. Similarly, other solid materials exhibit decreasing mechanical strength due to the high defect density in GBs.[99] Upon loadings, all polycrystals show a nonlinear behavior for the fraction of disorder water molecules as a function of the deformation strain. The change tendency

in the fraction of disordered water molecules is closely connected with deformation stages. In the first stage, no change in the fraction of disorder water molecules is observed, reflecting limited elastic responses. In the second stage, the fraction of disordered water molecules increases as the strain is increased, implying amorphization of crystalline water in polycrystals to accommodate the imposed strain. Such strain-induced amorphization does not lead to the decrease in strength but degradation in stiffness. Polycrystals are found to amorphize at the maximum damage rate as the stress reaches the yield point. Amorphization continues at a decreasing damage rate to critical points, which corresponds to the first part of strain-softening periods. In the remaining part of strain softening, for polycrystals with small grain size under tension, the fraction of disordered water tend to become a constant. Finally, slight reductions in disordered water are observed in the late deformation stage, implying crystallization occurring in polycrystals. In contrast, polycrystals with large grain size show an apparent decrease of disordered water in the following strain-softening stage, indicating large-scale recrystallization in this phase. Such significant recrystallization strengthens deformed polycrystals, resulting in strain hardening as shown in Figure 7a. However, polycrystals re-amorphize in the late deformation stage, as evidenced by the increasing fraction of disordered water in Figure 7e. Upon pressurization, polycrystals exhibit a similar trend for the fraction of disordered water in the late part of strain softening, except for polycrystal with a grain size of 10.58 nm that display an increase for the fraction of disordered water. In contrast to the case of tension, a linear enhancement in the fraction of disordered water is observed for all polycrsytals in the late straining, while polycrystals with large grain sizes demonstrate strain-softening behavior. This indicates that different deformation mechanisms govern the subsequent over-straining in polycrystals. The issue of an amorphous phase and failure strength in nanograined polycrystalline ice under extremely high strain rate is of importance for winter sports (ice-skating, bobsleighs, etc.), as certainly engineering and natural hazards if one thinks of hail stone impacts.

To further elucidate grain size-dependent mechanical responses from microscopic structures of polycrystals, a number of localized snapshots of polycrystals with two grain sizes upon different strains are captured and shown in Figure 8. Apparently, local crystalline textures in polycrystals change with the increase of both tensile and compressive strains. Figures 8a and 8b display the evolution of cross-sectional morphology of polycrystals with grain size of 7.94 and 15.87 nm under tension. Prior to yield strains, there is no GB sliding as evidenced by the highlighted solid segment which crosses GB. Crystalline grains are amorphous at the external surface to react to mechanical straining as indicated by the increasing fraction of disordered water (Figure 7e). Furthermore, minor structural transition from hexagonal to cubic phase locally occurs at high potential energy GBs. When the imposed strains exceed the yield values, collective GB sliding takes place to relax the strain energy as visually confirmed by the breaking of highlighted solid segment. This explains the observed strain-softening behavior as shown in Figure 7a. For polycrsytals with large grains, nanovoids are clearly nucleated at GB-surface multi-junctions, as a consequence of GB sliding that is non-accommodated. However, because of short-distance diffusion from GB to junctions, GB sliding is effectively accommodated by GB diffusion process, which leads to no apparent formation of nanovoids until large strains are imposed. Such nanovoid nucleation has been also observed in other solid materials.[120–122] At large strain of 0.24, minor cubic structure of ice is observed in the vicinity of multi-junctions in polycrystals with small grain size (Figure 8a-3), whereas for that with the largest grain size, a locally hexagonal-to-cubic structural transition occurring from multi-junction to interior grain is identified (Figure 8b-5). Upon compression, similar to the case of tension, no GB sliding occurs when the strains are below yield strains. However, changes in microstructure of GB are observed as shown by Figure 8c-1 and -2. Likewise, cooperative GB sliding happens to release the excess strain energy when the strains are beyond the yield points. In contrast to the case of tension, such large-scale GB sliding does not cause nucleation of nanovoids. With increase of compressive strain, structure geometry of some grains in polycrystals is greatly changed. As a consequence of high stress-concentration located at GBs that are perpendicular to loading direction, grains in polycrystals are greatly destabilized by amorphization, recrystallization, and phase transformation at GBs accompanied by roughening of the smooth GBs interfaces and rotation of grains (Figures 8c-3 and -6, d-3 and -6). Metals, upon heating and mechanical loading, are able to undergo such GB interface roughening transition.[123–125] Particularly, polycrystals with large grains show dislocation nucleation at the interior grains during
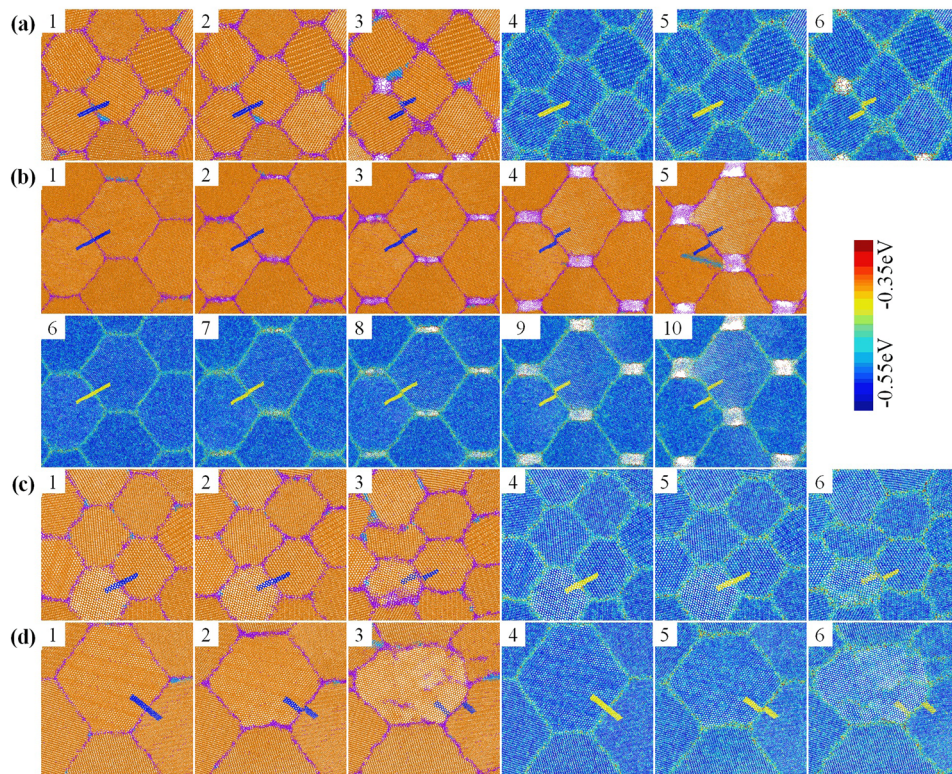
FIG. 8. Cross-sectional snapshots of polycrystalline I$_h$ under uniaxial loadings. (a) Polycrystals with grain size of 7.94 nm at tensile strains of 0.00, 0.06 and 0.24, respectively. (b) Polycrystals with grain size of 15.87 nm at tensile strains of 0.00, 0.06, 0.075, 0.15 and 0.24, respectively. (c) Polycrystals with grain size of 7.94 nm at compressive strains of 0.00, 0.06 and 0.24, respectively. (d) Polycrystals with a grain size of 15.87 nm at compressive strains of 0.00, 0.1 and 0.24, respectively. Water molecules in (a), (c) and (d) snapshots #1-3, and (b) snapshots #1-5 are colored according to their structural phases; Hexagonal, cubic and unidentified water structures are rendered by orange, light blue and purple, respectively. Water molecules in (a), (c) and (d) snapshots #4-6, and (b) snapshots #6-10 are colored based on their potential energy. Uniformly selected water particles are colored with either blue or yellow for monitoring GB sliding.

transgranular fracture of grains (Figure 8d-3), resulting in strength weakening of polycrystals as shown by the late strain-softening behavior in Figure 7b. This is the main source of the well-known classic Hall-Petch softening behavior in metals.[126] Experimentally, Schulson *et al.*[127] also showed that similar transgranular microcrack occurs in polycrystals composed of equiaxed and randomly oriented aggregates of granular ice, but those with small grains do not exhibit transgranular fracture behavior. Moreover, Duval *et al.*[67] reported that crystallographic slips govern mechanical deformation of polycrystalline ice and distribution of internal stress.

Some studies have been conducted to understand ice plasticity related to dislocation behaviors,[126,128–136] and dislocations have been richly studied in conventional solid materials.[137–141] To provide more information on dislocation in nanograined ice, snapshots of dislocation structures are captured. Figure 9 presents the simulated dislocation structures of polycrystalline ice with grain size of 15.87 nm. The results show rich dislocation behaviors in polycrystalline ice, consistent with the experimental observations.[126,128–132] A competition between dislocation-nucleation and dislocation-annihilation is found to occur during the entire deformation process. From Figure 9a, it is found that plenty of dislocations are uniformly distributed at GBs in the early deformation stage. However, in the strain-softening stage, dislocation nucleation activity is greatly weakened, but major $1/3\langle 1\,\bar{2}\,1\,0\rangle$ and minor $1/3\langle 1\,\bar{1}\,0\,0\rangle$ dislocation develop to form complex network topology in the entire polycrystal, as shown in Figure 9a-2. Using synchrotron X-ray topography, Liu *et al.*[130] also revealed that dislocations mainly nucleate at GBs of polycrystal with milimeter-sized grains, resulting in stiffness-softening. The change in dislocation type and location of dislocation nucleation implies the differences in plastic deformation modes between the two deformation stages. Figure 9b shows the
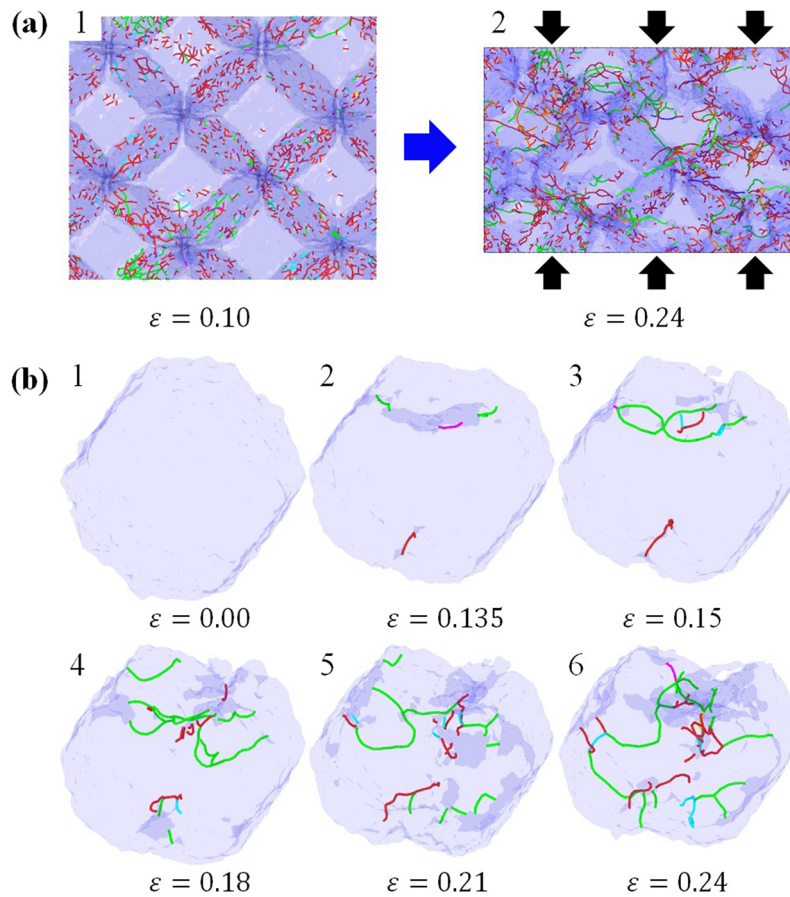
FIG. 9. Dislocation structures in polycrstalline I_h with grain size of 15.87 nm under compression. (a) Snapshots of dislocations occurring in nanograined polycrystal at two specific strains of 0.10 and 0.24. (b) Nucleation and propagation of dislocations in one typical nanograin that is selected from the polycrystal. Water molecules are removed for clarification. Dislocation segments are colored by the dislocation type, $1/3\langle 1\,\bar{2}\,1\,0\rangle$, $\langle 0\,0\,0\,1\rangle$, $\langle 1\,\bar{1}\,0\,0\rangle$, $1/3\langle 1\,\bar{1}\,0\,0\rangle$ and other are colored by green, yellow, pink, sky-blue and red, respectively.

detailed development of dislocation occurring in one grain. Initially, dislocations nucleate at the top and bottom damaged GBs that are perpendicular to loading direction. The top dislocations propagate and intersect to form a network motif, accompanied by new dislocations. Once the interaction between dislocation lines is turned on, dislocations come into being in the interior of grain. Meanwhile, the generation of new dislocations is also initiated at the bottom GB, and those dislocations propagate towards the interior of grain. Finally, dislocations coalesce to form complex dislocation network in the interior of grain to accommodate crystal deformation. However, among a variety of dislocations occurring in the interior of ice grain, screw dislocations with Burgers vector $1/3\langle 1\,\bar{2}\,1\,0\rangle$ are the most frequently observed as shown in Figure 9b. The similar dislocation behaviors have also been observed in hexagonal close-packed (HCP) solid materials.[137–141] Shōji *et al.*[142] reported that dislocation glide region in polycrystalline ice with grain size of 2 millimeters can be divided into dislocation glide with crack formation, dislocation creep, and fracture at high stresses. Similar to our findings, plastic deformation in twining-free polycrystalline metals with extremely fine grains was mostly governed by GBs.[105,143–145] Interplays between dislocations and GBs are utilized in GB engineering.[146] However, for nano-twinned polycrystalline metals, transition in plastic deformation mechanisms from dislocation pile-up and cutting through twin planes to a dislocation-nucleation-controlled softening mechanism with twin-boundary migration was revealed.[147] Dislocation behavior in polycrsytalline ice appears very complex, attributed to different mechanisms of generation and annihilation of dislocation. Importantly, plastic responses greatly depend on dislocation behaviors, which contain
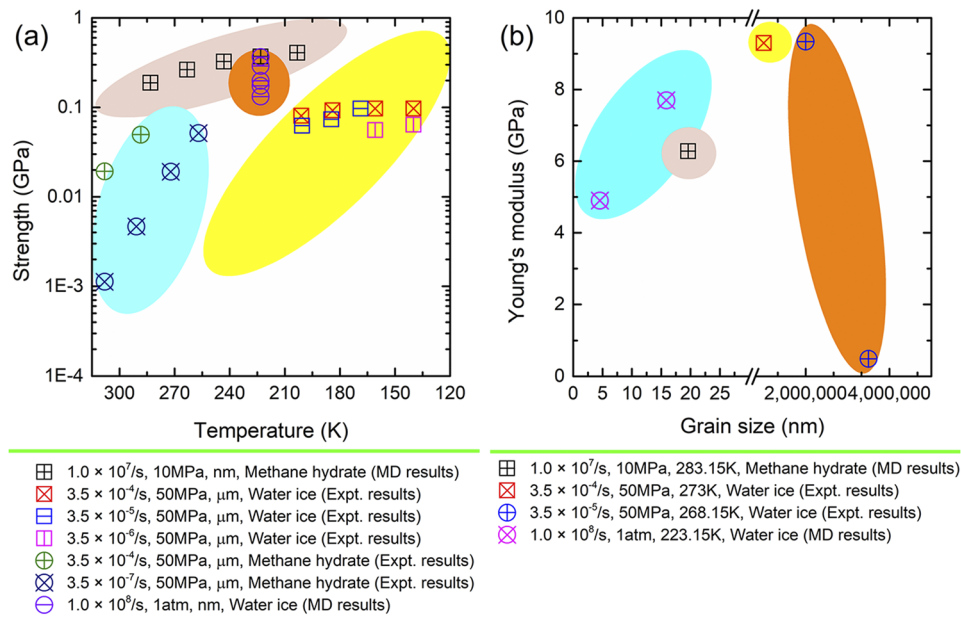
FIG. 10. Comparison of mechanical properties of ice and methane hydrate. (a) Maximum strength of both polycrystals as a function of temperature. (b) Young's modulus of both polycrystals as a function of grain size. The corresponding experimental data for both water ice and methane clathrate are compared.[31,47,82,113–117]

mutual interactions between dislocations, interactions between dislocations and other defects such as GBs.

III. CONCLUSIONS

In summary, large-scale classical MD simulations with the coarse-grained mW water model were performed to reveal failure and deformation mechanism of bi-, and poly-crystalline I_h under mechanical loads. For bicrystals, a series of tension, compression and shear MD tests reveal that mechanical characteristics, such as elastic moduli, ultimate strength, failure modes and dislocation behaviors, strongly depend on GB structures that are determined by the plane of jointed monocrystals. MD simulations of polycrystals with extremely fine grains subjected to both tensile and compressive loads demonstrate pronounced grain size effect on mechanical behaviors. Both the yield stress and flow stress decrease with grain size under the simulation conditions, which is similar to the inverse Hall-Petch behavior observed in other polycrystalline textured materials. The high ratio of amorphous crystalline water molecules in polycrystal with small grain size is responsible for the inverse Hall-Petch softening. Mechanical plastic deformation of ice polycrystal is found to be cooperatively governed by strain-induced amorphization and recrystallization, GB sliding, dislocation nucleations, phase transformation, GB roughening and grain rotation. This study provides key insights into the structural, failure and plasticity of solid water ice, shedding light on the distinct deformation mechanism of water ice at the nanoscale.

ACKNOWLEDGMENTS

[1] A. Falenty, T. C. Hansen, and W. F. Kuhs, "Formation and properties of ice XVI obtained by emptying a type sII clathrate hydrate," Nature **516**(7530), 231–233 (2014).

[2] E. M. Schulson, "The structure and mechanical behavior of ice," JOM Journal of the Minerals Metals and Materials Society **51**(2), 21–27 (1999).

[3] T. Bartels-Rausch, V. Bergeron, J. H. E. Cartwright, R. Escribano, J. L. Finney, H. Grothe, P. J. Gutiérrez, J. Haapala, W. F. Kuhs, J. B. C. Pettersson, S. D. Price, C. I. Sainz-Díaz, D. J. Stokes, G. Strazzulla, E. S. Thomson, H. Trinks, and N. Uras-Aytemiz, "Ice structures, patterns, and processes: A view across the icefields," Reviews of Modern Physics **84**(2), 885–944 (2012).

[4] C. Lobban, J. L. Finney, and W. F. Kuhs, "The structure of a new phase of ice," Nature **391**(6664), 268–270 (1998).

[5] N. Bjerrum, "Structure and properties of ice," Science **115**(2989), 385–390 (1952).

[6] W. H. Barnes, "The crystal structure of ice between 0°C. And -183°C," Proceedings of the Royal Society of London. Series A, Containing Papers of a Mathematical and Physical Character **125**(799), 670–693 (1929).

[7] A. Goto, T. Hondoh, and S. Mae, "The electron density distribution in ice Ih determined by single-crystal x-ray diffractometry," The Journal of Chemical Physics **93**(2), 1412 (1990).

[8] M. Matsumoto, S. Saito, and I. Ohmine, "Molecular dynamics simulation of the ice nucleation and growth process leading to water freezing," Nature **416**(6879), 409–413 (2002).

[9] E. B. Moore and V. Molinero, "Structural transformation in supercooled water controls the crystallization rate of ice," Nature **479**(7374), 506–508 (2011).

[10] C. Hoose, J. E. Kristjánsson, J.-P. Chen, and A. Hazra, "A classical-theory-based parameterization of heterogeneous ice nucleation by mineral dust, soot, and biological particles in a global climate model," Journal of the Atmospheric Sciences **67**(8), 2483–2503 (2010).

[11] D. A. Knopf and T. Koop, "Heterogeneous nucleation of ice on surrogates of mineral dust," Journal of Geophysical Research: Atmospheres **111**, D12201, https://doi.org/10.1029/2005jd006894 (2006).

[12] A. J. Durant, R. A. Shaw, W. I. Rose, Y. Mi, and G. G. J. Ernst, "Ice nucleation and overseeding of ice in volcanic clouds," Journal of Geophysical Research: Atmospheres **113**, D09206, https://doi.org/10.1029/2007jd009064 (2008).

[13] P. J. DeMott, "An exploratory study of ice nucleation by soot aerosols," Journal of Applied Meteorology **29**(10), 1072–1079 (1990).

[14] B. Kärcher and U. Lohmann, "A parameterization of cirrus cloud formation: Homogeneous freezing of supercooled aerosols," Journal of Geophysical Research: Atmospheres **107**(D2), AAC 4-1–AAC 4-10, https://doi.org/10.1029/2001jd000470 (2002).

[15] B. Krämer, O. Hübner, H. Vortisch, L. Wöste, T. Leisner, M. Schwell, E. Rühl, and H. Baumgärtel, "Homogeneous nucleation rates of supercooled water measured in single levitated microdroplets," The Journal of Chemical Physics **111**(14), 6521–6527 (1999).

[16] T. Li, D. Donadio, G. Russo, and G. Galli, "Homogeneous ice nucleation from supercooled water," Physical Chemistry Chemical Physics **13**(44), 19807–19813 (2011).

[17] A. Tabazadeh, Y. S. Djikaev, and H. Reiss, "Surface crystallization of supercooled water in clouds," Proceedings of the National Academy of Sciences **99**(25), 15873–15878 (2002).

[18] T. Koop, B. Luo, A. Tsias, and T. Peter, "Water activity as the determinant for homogeneous ice nucleation in aqueous solutions," Nature **406**(6796), 611–614 (2000).

[19] S. Hartmann, D. Niedermeier, J. Voigtländer, T. Clauss, R. Shaw, H. Wex, A. Kiselev, and F. Stratmann, "Homogeneous and heterogeneous ice nucleation at LACIS: Operating principle and theoretical studies," Atmospheric Chemistry and Physics **11**(4), 1753–1767 (2011).

[20] W. Cantrell and A. Heymsfield, "Production of ice in tropospheric clouds: A review," Bulletin of the American Meteorological Society **86**(6), 795–808 (2005).

[21] R. P. Sear, "Quantitative studies of crystal nucleation at constant supersaturation: Experimental data and models," CrystEngComm **16**(29), 6506–6522 (2014).

[22] H. Pruppacher, J. Klett, and P. Wang, "Microphysics of clouds and precipitation," Aerosol Science & Technology **28**(4), 381–382 (1997).

[23] O. Mishima, L. D. Calvert, and E. Whalley, "An apparently first-order transition between two amorphous phases of ice induced by pressure," Nature **314**(6006), 76–78 (1985).

[24] O. Mishima, L. D. Calvert, and E. Whalley, "'Melting ice' I at 77 K and 10 kbar: A new method of making amorphous solids," Nature **310**(5976), 393–395 (1984).

[25] J. S. Tse, "Mechanical instability in ice Ih. A mechanism for pressure-induced amorphization," The Journal of Chemical Physics **96**(7), 5482 (1992).

[26] R. Andrews, "Measurement of the fracture toughness of glacier ice," Journal of Glaciology **31**(108), 171–176 (1985).

[27] N. Reeh, H. H. Thomsen, A. K. Higgins, and A. Weidick, "Sea ice and the stability of north and northeast Greenland floating glaciers," Annals of Glaciology **33**(1), 474–480 (2001).

[28] R. Thomas, E. Frederick, J. Li, W. Krabill, S. Manizade, J. Paden, J. Sonntag, R. Swift, and J. Yungel, "Accelerating ice loss from the fastest Greenland and Antarctic glaciers," Geophysical Research Letters **38**, L10502, https://doi.org/10.1029/2011gl047304 (2011).

[29] T. D. Prowse, "Environmental significance of ice to streamflow in cold regions," Freshwater Biology **32**(2), 241–259 (1994).

[30] J. B. Murton, R. Peterson, and J.-C. Ozouf, "Bedrock fracture by ice segregation in cold regions," Science **314**(5802), 1127 (2006).

[31] J. Currier and E. Schulson, "The tensile strength of ice as a function of grain size," Acta Metallurgica **30**(8), 1511–1514 (1982).

[32] R. W. Lee and E. Schulson, "The strength and ductility of ice under tension," Journal of Offshore Mechanics and Arctic Engineering **110**(2), 187–191 (1988).

[33] B. Michel, "The strength of polycrystalline ice," Canadian Journal of Civil Engineering **5**(3), 285–300 (1978).

[34] M. Shazly, V. Prakash, and B. A. Lerch, "High strain-rate behavior of ice under uniaxial compression," International Journal of Solids and Structures **46**(6), 1499–1515 (2009).

[35] L. W. Gold, "On the elasticity of ice plates," Canadian Journal of Civil Engineering **15**(6), 1080–1084 (1988).

[36] W. F. Weeks and D. L. Anderson, "An experimental study of strength of young sea ice," Transactions American Geophysical Union **39**(4), 641–647 (1958).

[37] F. Haynes, "Effect of temperature on the strength of snow-ice," Cold Regions Research and Engineering Laboratory, CRREL Report, 78-27 (1978).

[38] X. Xian, M. Chu, R. Scavuzzo, and T. Srivatsan, "An experimental evaluation of the tensile strength of impact ice," Journal of Materials Science Letters **8**(10), 1205–1208 (1989).

[39] E. M. Schulson, S. G. Hoxie, and W. A. Nixon, "The tensile strength of cracked ice," Philosophical Magazine A **59**(2), 303–311 (1989).

[40] D. L. Bentley, J. P. Dempsey, D. S. Sodhi, and Y. Wei, "Fracture toughness of columnar freshwater ice from large scale DCB tests," Cold Regions Science and Technology **17**(1), 7–20 (1989).

[41] W. Nixon and E. Schulson, "A micromechanical view of the fracture toughness of ice," Le Journal de Physique Colloques **48**(C1), C1-313–C311-319 (1987).

[42] M. P. Fischer, R. B. Alley, and T. Engelder, "Fracture toughness of ice and firn determined from the modified ring test," Journal of Glaciology **41**(138), 383–394 (1995).

[43] L. Weber and W. Nixon, "Fracture toughness of freshwater ice—Part I: Experimental technique and results," Journal of Offshore Mechanics and Arctic Engineering **118**(2), 135–140 (1996).

[44] T. Uchida and S. Kusumoto, "Effects of test conditions on fracture toughness and fracture morphology of polycrystalline ice," JSME International Journal Series A Solid Mechanics and Material Engineering **42**(4), 601–609 (1999).

[45] I. Hawkes and M. Mellor, "Deformation and fracture of ice under uniaxial stress," Journal of Glaciology **11**(61), 103–131 (1972).

[46] J. Druez, J. L. Laforte, and C. Tremblay, "Experimental results on the tensile strength of atmospheric ice," Transactions of the Canadian Society for Mechanical Engineering **13**(3), 59–64 (1989).

[47] D. M. Cole, "Strain-rate and grain-size effects in ice," Journal of Glaciology **33**(115), 274–280 (1987).

[48] A. Godio and R. B. Rege, "The mechanical properties of snow and ice of an alpine glacier inferred by integrating seismic and GPR methods," Journal of Applied Geophysics **115**, 92–99 (2015).

[49] N. Fletcher, *The Chemical Physics of Ice* (Cambridge University Press, London Cambridge, 1970).

[50] Z. M. Jendi, P. Servio, and A. D. Rey, "Ideal strength of methane hydrate and ice I$_h$ from first-principles," Crystal Growth & Design **15**(11), 5301–5309 (2015).

[51] L. W. Gold, "Some observations on the dependence of strain on stress for ice," Canadian Journal of Physics **36**(10), 1265–1275 (1958).

[52] W. F. Waite, M. B. Helgerud, A. Nur, J. C. Pinkston, L. A. Stern, S. H. Kirby, and W. B. Durham, "Laboratory measurements of compressional and shear wave speeds through methane hydrate," Annals of the New York Academy of Sciences **912**(1), 1003–1010 (1999).

[53] G. W. Timco and W. F. Weeks, "A review of the engineering properties of sea ice," Cold Regions Science and Technology **60**(2), 107–129 (2010).

[54] D. L. Anderson and W. F. Weeks, "A theoretical analysis of sea–ice strength," Transactions American Geophysical Union **39**(4), 632–640 (1958).

[55] M. Langleben, "Young's modulus for sea ice," Canadian Journal of Physics **40**(1), 1–8 (1962).

[56] A. A. Elvin, "Number of grains required to homogenize elastic properties of polycrystalline ice," Mechanics of Materials **22**(1), 51–64 (1996).

[57] R. L. Hooke, M. Mellor, W. Budd, J. Glen, A. Higashi, T. Jacka, S. Jones, R. Lile, R. Martin, and M. Meier, "Mechanical properties of polycrystalline ice: An assessment of current knowledge and priorities for research: Report prepared for the International Commission on snow and ice, with support from the US National Science Foundation," Cold Regions Science and Technology **3**(4), 263–275 (1980).

[58] A. M. A. Mohamed and M. Farzaneh, "An experimental study on the tensile properties of atmospheric ice," Cold Regions Science and Technology **68**(3), 91–98 (2011).

[59] V. Gupta and P. Archer, "Measurement of the grain-boundary tensile strength in columnar freshwater ice," Philosophical Magazine Letters **79**(8), 503–509 (2010).

[60] E. M. Schulson, "The brittle compressive fracture of ice," Acta Metallurgica et Materialia **38**(10), 1963–1976 (1990).

[61] M. S. Wu and J. Niu, "Micromechanical prediction of the compressive failure of ice: Model development," Mechanics of Materials **20**(1), 9–32 (1995).

[62] S. J. Jones and H. A. M. Chew, "Effect of sample and grain size on the compressive strength of ice," Annals of Glaciology **4**, 129–132 (1983).

[63] S. J. Jones and H. A. M. Chew, "On the grain-size dependence of secondary creep," Journal of Glaciology **27**(97), 517–518 (1981).

[64] W. F. Budd and T. H. Jacka, "A review of ice rheology for ice sheet modelling," Cold Regions Science and Technology **16**(2), 107–144 (1989).

[65] T. H. Jacka, "Laboratory studies on relationships between ice crystal size and flow rate," Cold Regions Science and Technology **10**(1), 31–42 (1984).

[66] T. H. Jacka and M. Maccagnan, "Ice crystallographic and strain rate changes with strain in compression and extension," Cold Regions Science and Technology **8**(3), 269–286 (1984).

[67] P. Duval, M. F. Ashby, and I. Anderman, "Rate-controlling processes in the creep of polycrystalline ice," The Journal of Physical Chemistry **87**(21), 4066–4074 (1983).

[68] J. Muguruma, "Effects of surface condition on the mechanical properties of ice crystals," Journal of Physics D: Applied Physics **2**(11), 1517 (1969).

[69] J. W. Glen, "The creep of polycrystalline ice," Proceedings of the Royal Society of London. Series A. Mathematical and Physical Sciences **228**(1175), 519–538 (1955).

[70] J. R. Stokes, J. H. Telford, and A.-M. Williamson, "The flowability of ice suspensions," Journal of Rheology **49**(1), 139–148 (2005).

[71] C. R. Stokes, M. Spagnolo, C. D. Clark, C. Ó. Cofaigh, O. B. Lian, and R. B. Dunstone, "Formation of mega-scale glacial lineations on the Dubawnt Lake ice stream bed: 1. Size, shape and spacing from a large remote sensing dataset," Quaternary Science Reviews **77**, 190–209 (2013).

[72] C. R. Stokes and C. D. Clark, "Are long subglacial bedforms indicative of fast ice flow?," Boreas **31**(3), 239–249 (2008).

[73] D. L. Goldsby and D. L. Kohlstedt, "Superplastic deformation of ice: Experimental observations," Journal of Geophysical Research: Solid Earth **106**(B6), 11017–11030, https://doi.org/10.1029/2000jb900336 (2001).

[74] A. K. Sum, C. A. Koh, and E. D. Sloan, "Clathrate hydrates: From laboratory science to engineering practice," Industrial & Engineering Chemistry Research **48**(16), 7457–7465 (2009).

[75] M. Dao, L. Lu, R. J. Asaro, J. T. M. De Hosson, and E. Ma, "Toward a quantitative understanding of mechanical behavior of nanocrystalline metals," Acta Materialia **55**(12), 4041–4065 (2007).

[76] J. Bernal and R. Fowler, "A theory of water and ionic solution, with particular reference to hydrogen and hydroxyl ions," The Journal of Chemical Physics **1**(8), 515–548 (1933).

[77] W. Brostow, J.-P. Dussault, and B. L. Fox, "Construction of Voronoi polyhedra," Journal of Computational Physics **29**(1), 81–92 (1978).

[78] J. L. Finney, "A procedure for the construction of Voronoi polyhedra," Journal of Computational Physics **32**(1), 137–143 (1979).

[79] F. H. Stillinger and T. A. Weber, "Computer simulation of local order in condensed phases of silicon," Physical Review B **31**(8), 5262–5271 (1985).

[80] V. Molinero and E. B. Moore, "Water modeled as an intermediate element between carbon and silicon," Journal of Physical Chemistry B **113**(13), 4008–4016 (2009).

[81] L. C. Jacobson and V. Molinero, "A methane-water model for coarse-grained simulations of solutions and clathrate hydrates," Journal of Physical Chemistry B **114**(21), 7302–7311 (2010).

[82] J. Wu, F. Ning, T. T. Trinh, S. Kjelstrup, T. J. H. Vlugt, J. He, B. H. Skallerud, and Z. Zhang, "Mechanical instability of monocrystalline and polycrystalline methane hydrates," Nature Communications **6**, 8743 (2015).

[83] E. Polak and G. Ribière, "Note sur la convergence de methodes de directions conjugées," Rev. Francaise Inf. Rech. Opér. **16**, 35–43 (1969).

[84] S. Plimpton, "Fast parallel algorithms for short-range molecular dynamics," Journal of Computational Physics **117**(1), 1–19 (1995).

[85] E. Maras, O. Trushin, A. Stukowski, T. Ala-Nissila, and H. Jónsson, "Global transition path search for dislocation formation in Ge on Si(001)," Computer Physics Communications **205**, 13–21 (2016).

[86] D. S. Franzblau, "Computation of ring statistics for network models of solids," Physical Review B **44**(10), 4925–4930 (1991).

[87] S. Alexander, V. B. Vasily, and A. Athanasios, "Automated identification and indexing of dislocations in crystal interfaces," Modelling and Simulation in Materials Science and Engineering **20**(8), 085007 (2012).

[88] K. Mochizuki, M. Matsumoto, and I. Ohmine, "Defect pair separation as the controlling step in homogeneous ice melting," Nature **498**(7454), 350–354 (2013).

[89] D. J. Brockwell, E. Paci, R. C. Zinober, G. S. Beddard, P. D. Olmsted, D. A. Smith, R. N. Perham, and S. E. Radford, "Pulling geometry defines the mechanical resistance of a β-sheet protein," Nature Structural & Molecular Biology **10**(9), 731–737 (2003).

[90] M. Rief, M. Gautel, F. Oesterhelt, J. M. Fernandez, and H. E. Gaub, "Reversible unfolding of individual titin immunoglobulin domains by AFM," Science **276**(5315), 1109 (1997).

[91] X. Liu, Q. S. Yang, X. Q. He, and Y. W. Mai, "Molecular mechanics modeling of deformation and failure of super carbon nanotube networks," Nanotechnology **22**(47), 475701 (2011).

[92] S. Maity, M. Mazzolini, M. Arcangeletti, A. Valbuena, P. Fabris, M. Lazzarino, and V. Torre, "Conformational rearrangements in the transmembrane domain of CNGA1 channels revealed by single-molecule force spectroscopy," Nature Communications **6**, 7093 (2015).

[93] K. Morishige and H. Uematsu, "The proper structure of cubic ice confined in mesopores," The Journal of Chemical Physics **122**(4), 044711 (2005).

[94] E. Mayer and A. Hallbrucker, "Cubic ice from liquid water," Nature **325**(6105), 601–602 (1987).

[95] I. Kohl, E. Mayer, and A. Hallbrucker, "The glassy water–cubic ice system: A comparative study by X-ray diffraction and differential scanning calorimetry," Physical Chemistry Chemical Physics **2**(8), 1579–1586 (2000).

[96] A. Elarby-Aouizerat, J.-F. Jal, J. Dupuy, H. Schildberg, and P. Chieux, "Comments on the ice Ic structure and Ic to Ih phase transformation mechanism: A neutron scattering investigation of ice precipitates in glassy LiCl. D_2O," Le Journal de Physique Colloques **48**(C1), C1-465–C461-470 (1987).

[97] D. Donadio, P. Raiteri, and M. Parrinello, "Topological defects and bulk melting of hexagonal ice," The Journal of Physical Chemistry B **109**(12), 5421–5424 (2005).

[98] N. Grishina and V. Buch, "Structure and dynamics of orientational defects in ice I," The Journal of Chemical Physics **120**(11), 5217–5225 (2004).

[99] Y. Wei, J. Wu, H. Yin, X. Shi, R. Yang, and M. Dresselhaus, "The nature of strength enhancement and weakening by pentagon–heptagon defects in graphene," Nature Materials **11**(9), 759 (2012).

[100] Y. Bi, B. Cao, and T. Li, "Enhanced heterogeneous ice nucleation by special surface geometry," Nature Communications **8**, 15372 (2017).

[101] M. B. Helgerud, W. F. Waite, S. H. Kirby, and A. Nur, "Elastic wave speeds and moduli in polycrystalline ice Ih, sI methane hydrate, and sII methane-ethane hydrate," Journal of Geophysical Research: Solid Earth **114**(B2), n/a–n/a, https://doi.org/10.1029/2008jb006132 (2009).

[102] J. Jia, Y. Liang, T. Tsuji, S. Murata, and T. Matsuoka, "Microscopic origin of strain hardening in methane hydrate," Scientific Reports **6**, 23548 (2016).

[103] L. A. Stern, W. B. Durham, and S. H. Kirby, "Grain-size-induced weakening of H_2O ices I and II and associated anisotropic recrystallization," Journal of Geophysical Research: Solid Earth **102**(B3), 5313–5325, https://doi.org/10.1029/96jb03894 (1997).

[104] D. M. Cole, "Grain size and the compressive strength of ice," Journal of Energy Resources Technology **107**(3), 369–374 (1985).

[105] J. Schiotz, F. D. Di Tolla, and K. W. Jacobsen, "Softening of nanocrystalline metals at very small grain sizes," Nature **391**(6667), 561–563 (1998).

[106] J. Schiøtz and K. W. Jacobsen, "A maximum in the strength of nanocrystalline copper," Science **301**(5638), 1357 (2003).

[107] E. C. Pettit and E. D. Waddington, "Ice flow at low deviatoric stress," Journal of Glaciology **49**(166), 359–369 (2003).

[108] J. R. Greer, D. Jang, and X. W. Gu, "Exploring deformation mechanisms in nanostructured materials," JOM Journal of the Minerals Metals and Materials Society **64**(10), 1241–1252 (2012).

[109] J. R. Greer, "Nanotwinned metals: It's all about imperfections," Nature Materials **12**(8), 689–690 (2013).

[110] B. Vorselaars, A. V. Lyulin, and M. Michels, "Deforming glassy polystyrene: Influence of pressure, thermal history, and deformation mode on yielding and hardening," The Journal of Chemical Physics **130**(7), 074905 (2009).

[111] J. Liu, S. Wu, L. Zhang, W. Wang, and D. Cao, "Molecular dynamics simulation for insight into microscopic mechanism of polymer reinforcement," Physical Chemistry Chemical Physics **13**(2), 518–529 (2011).

[112] T. Jiang, L. Wang, and J. Lin, "Distinct mechanical properties of nanoparticle-tethering polymers," RSC Advances **4**(67), 35272–35283 (2014).

[113] F. Ning, Y. Yu, S. Kjelstrup, T. J. H. Vlugt, and K. Glavatskiy, "Mechanical properties of clathrate hydrates: Status and perspectives," Energy & Environmental Science **5**(5), 6779–6795 (2012).

[114] L. A. Stern, S. H. Kirby, and W. B. Durham, "Peculiarities of methane clathrate hydrate formation and solid-state deformation, including possible superheating of water ice," Science **273**, 1843–1848 (1996).

[115] L. A. Stern, S. H. Kirby, and W. B. Durham, "Polycrystalline methane hydrate: Synthesis from superheated ice, and low-temperature mechanical properties," Energy & Fuels **12**(2), 201–211 (1998).

[116] W. B. Durham, S. H. Kirby, L. A. Stern, and W. Zhang, "The strength and rheology of methane clathrate hydrate," Journal of Geophysical Research: Solid Earth **108**(B4), https://doi.org/10.1029/2002jb001872 (2003).

[117] W. B. Durham and L. A. Stern, "Rheological properties of water ice-applications to satellites of the outer planets," Annual Review of Earth and Planetary Sciences **29**, 295–330 (2001).

[118] Y. J. Wei and L. Anand, "Grain-boundary sliding and separation in polycrystalline metals: Application to nanocrystalline fcc metals," Journal of the Mechanics and Physics of Solids **52**(11), 2587–2616 (2004).

[119] P. Cao, J. Wu, Z. Zhang, and F. Ning, "Mechanical properties of monocrystalline and polycrystalline monolayer black phosphorus," Nanotechnology **28**(4), 045702 (2016).

[120] A. H. Chokshit and A. K. Mukherjee, "An analysis of cavity nucleation in superplasticity," Acta Metallurgica **37**(11), 3007–3017 (1989).

[121] C. Reina, J. Marian, and M. Ortiz, "Nanovoid nucleation by vacancy aggregation and vacancy-cluster coarsening in high-purity metallic single crystals," Physical Review B **84**(10), 104117 (2011).

[122] R. L. Narayan, P. Tandaiya, R. Narasimhan, and U. Ramamurty, "Wallner lines, crack velocity and mechanisms of crack nucleation and growth in a brittle bulk metallic glass," Acta Materialia **80**, 407–420 (2014).

[123] X. Huang, N. Hansen, and N. Tsuji, "Hardening by annealing and softening by deformation in nanostructured metals," Science **312**(5771), 249 (2006).

[124] K. Lu, "Stabilizing nanostructures in metals using grain and twin boundary architectures," Nature Reviews Materials **1**, 16019 (2016).

[125] T. H. Fang, W. L. Li, N. R. Tao, and K. Lu, "Revealing extraordinary intrinsic tensile plasticity in gradient nano-grained copper," Science **331**(6024), 1587 (2011).

[126] F. Liu, I. Baker, and M. Dudley, "Dislocation-grain boundary interactions in ice crystals," Philosophical Magazine A **71**(1), 15–42 (1995).

[127] E. M. Schulson, I. Baker, C. D. Robertson, R. B. Bolon, and R. J. Harnimon, "Fractography of ice," Journal of Materials Science Letters **8**(10), 1193–1194 (1989).

[128] I. Weikusat, D. A. M. De Winter, G. M. Pennock, M. Hayles, C. T. W. M. Schneijdenberg, and M. R. Drury, "Cryogenic EBSD on ice: Preserving a stable surface in a low pressure SEM," Journal of Microscopy **242**(3), 295–310 (2011).

[129] W. W. Webb and C. E. Hayes, "Dislocations and plastic deformation of ice," Philosophical Magazine **16**(143), 909–925 (1967).

[130] F. Liu, I. Baker, and M. Dudley, "Dynamic observations of dislocation generation at grain boundaries in ice," Philosophical Magazine A **67**(5), 1261–1276 (1993).

[131] I. Baker, "Examination of dislocations in ice," Crystal Growth & Design **2**(2), 127–134 (2002).

[132] C. Shearwood and R. W. Whitworth, "Novel processes of dislocation multiplication observed in ice," Acta Metallurgica et Materialia **41**(1), 205–210 (1993).

[133] C. Hayes and W. Webb, "Dislocations in ice," Science **147**(3653), 44–45 (1965).

[134] S. Ahmad and R. W. Whitworth, "Dislocation motion in ice: A study by synchrotron X-ray topography," Philosophical Magazine A **57**(5), 749–766 (1988).

[135] J. W. Glen, "The effect of hydrogen disorder on dislocation movement and plastic deformation of ice," Physik der Kondensierten Materie **7**(1), 43–51 (1968).

[136] R. W. Whitworth, "Velocity of dislocations in ice on {0001} and {1010} planes," The Journal of Physical Chemistry **87**(21), 4074–4078 (1983).

[137] E. Clouet, "Screw dislocation in zirconium: An ab initio study," Physical Review B **86**(14), 144104 (2012).

[138] M. H. Yoo, "Slip, twinning, and fracture in hexagonal close-packed metals," Metallurgical Transactions A **12**(3), 409–418 (1981).

[139] G. Monnet, B. Devincre, and L. P. Kubin, "Dislocation study of prismatic slip systems and their interactions in hexagonal close packed metals: Application to zirconium," Acta Materialia **52**(14), 4317–4328 (2004).

[140] M. H. Yoo and C. T. Wei, "Slip modes of hexagonal-close-packed metals," Journal of Applied Physics **38**(11), 4317–4322 (1967).

[141] N. Chaari, E. Clouet, and D. Rodney, "First order pyramidal slip of 1/3<1 -2 1 0> screw dislocations in zirconium," Metallurgical and Materials Transactions A **45**(13), 5898–5905 (2014).

[142] H. Shōji and A. Higashi, "A deformation mechanism map of ice," Journal of Glaciology **21**(85), 419–427 (1978).

[143] S. Yip, "Nanocrystals: The strongest size," Nature **391**(6667), 532–533 (1998).

[144] H. Van Swygenhoven, M. Spaczer, A. Caro, and D. Farkas, "Competing plastic deformation mechanisms in nanophase metals," Physical Review B **60**(1), 22–25 (1999).

[145] H. Van Swygenhoven, "Grain boundaries and dislocations," Science **296**(5565), 66 (2002).

[146] V. Randle, "Mechanism of twinning-induced grain boundary engineering in low stacking-fault energy materials," Acta Materialia **47**(15–16), 4187–4196 (1999).

[147] X. Li, Y. Wei, L. Lu, K. Lu, and H. Gao, "Dislocation nucleation governed softening and maximum strength in nano-twinned metals," Nature **464**(7290), 877–880 (2010).